

A Study of Static and Dynamic Robustness of Hydro/Omniphobic Surfaces

by

Kyoo Chul Park

B.S. Department of Mechanical and Aerospace Engineering
Seoul National University, 2008

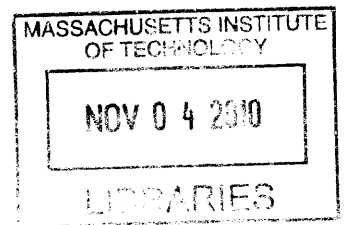
Submitted to the Department of Mechanical Engineering
in partial fulfillment of the requirements for the Degree of
Master of Science in Mechanical Engineering

at the

Massachusetts Institute of Technology

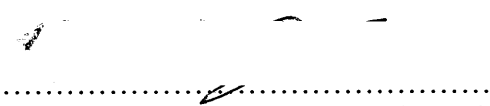
September 2010

© 2010 Massachusetts Institute of Technology.
All rights reserved.

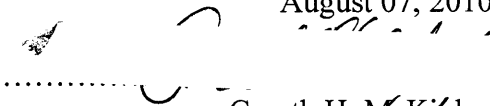


ARCHIVES

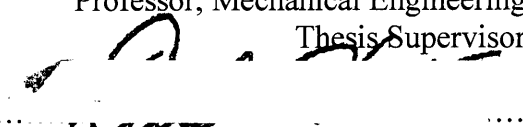
Signature of Author.....


Kyoo-Chul (Kenneth) Park
Department of Mechanical Engineering
August 07, 2010

Certified by.....


Gareth H. McKinley
Professor, Mechanical Engineering
Thesis Supervisor

Accepted by.....


David E. Hardt
Professor, Mechanical Engineering
Chairman, Graduate Thesis Committee

A Study of Static and Dynamic Robustness of Hydro/Omniphobic Surfaces

by

Kyoo Chul Park

Submitted to the Department of Mechanical Engineering
on August 7, 2010, in partial fulfillment of
the requirements for the Degree of
Master of Science in Mechanical Engineering

Abstract

Liquid droplets in the Cassie-Baxter state form liquid-air interfaces that are not flat but distorted due to pressure differences across the interfaces between the asperities. These distorted interfaces play an essential role in the transition from the composite Cassie-Baxter state to the fully-wetted Wenzel state and in the determination of the robustness of the composite state. As well as the static pressure difference due to the Laplace pressure, dynamic pressure difference due to various configurations including drop impact is also a source that causes the transition with the distorted interfaces. However, there are few experimental and numerical studies that consider the details of the distorted interfaces for a wide range of liquids and there is a lack of an *a priori* method to evaluate the robustness of three-dimensionally complicated textures. In addition, previous studies on drop impact pressure did not cover the maximum pressure at impact in the range of low velocities (< 2 m/s). We have first investigated the shape of distorted liquid-air interfaces and their transition conditions experimentally by using droplets of various low surface tension liquids on millimeter-sized re-entrant surface topography. For the dynamic pressure difference, we proposed a modified water hammer pressure formula and compared with the experiment using a high speed camera. The static experimental results by using three dimensionally printed millimetric structures are in good agreement with our newly-developed finite element simulations. These three-dimensional simulations of the interfacial shape provide a predictive tool for the robustness of a wide range of proposed micro-texture in terms of the breakthrough pressure at which the distorted liquid-air interface infiltrate into the space between asperities and the droplet transitions to the Wenzel state. The dynamic experimental results open a broad avenue to a novel approach to delve into the dynamic breakthrough pressure of droplets of a variety of liquids.

Thesis Supervisor: Gareth H. McKinley
Title: Professor, Mechanical Engineering

Acknowledgements

First and foremost, I would like to thank Professor Gareth H. McKinley, my thesis advisor, for his guidance, support, patience, enthusiasm and attention. Owing to his leadership, I have learned to see a bigger picture, changing my way of thinking.

None of the works in this thesis would have been possible without the help of many people at the MIT. I would like to thank Professor Robert E. Cohen and Dr. Wonjae Choi for their guidance, enthusiasm and dedication to this study. I would also like to thank Shreerang S. Chhatre, Dr. Adam Meuler and Professor Anish Tuteja for their valuable advice and help regarding the experimental works. Dr. Vivek Sharma and Dr. Johannes Soulages, the lab members deserve special mention for providing advice and guidance in the academia and theories in the wetting and drop impact study as well as the fabrication of textured surfaces. I would like to mention the help of Sangok Seok for the development of the drop impact measurement system using LabVIEW™. I would also like to thank Cambridge Scholarship Foundation for supporting my study and research at MIT, and both Air Force Research Lab and Xerox Research Center for their funding for the research on non-wetting surfaces.

I would like to thank my colleagues of the Non-Newtonian Fluid Dynamics Lab and at the MIT, especially Thomas Ober, Sarah W. Bates, Christopher Dimitriou, Dr. Randy H. Ewoldt, and other lab members for their invaluable advices and support. Special thanks to my family, father, Chan Jo Park, my mother, Jae Nam Gil, and my brother, Jong Sun Park and my friends for their unlimited mental support.

Contents

1. INTRODUCTION.....	15
1.1 MOTIVATION: HYDROPHOBIC AND OMNIPHOBIC SURFACES	15
1.2 LITERATURE REVIEW	18
1.2.1 <i>Equilibrium contact angle and apparent contact angle</i>	18
1.2.2 <i>Re-entrant structure</i>	21
1.2.3 <i>Thermodynamics - metastable composite state</i>	24
1.2.4 <i>Robustness of the composite state</i>	26
1.2.5 <i>Numerical calculations of breakthrough pressure</i>	30
1.2.6 <i>Drop impact pressure</i>	32
1.3 APPLICATIONS AND ROBUSTNESS PROBLEMS	33
1.4 OBJECTIVES AND APPROACH	35
1.5 CHAPTER DESCRIPTION	37
2. METHODOLOGY.....	39
2.1 FABRICATION OF MILLIHOODOOS	39
2.1.1 <i>Three-dimensional printing</i>	39
2.1.2 <i>Dip Coating</i>	41
2.2 SURFACE EVOLVER	42
2.3 REPLICATION PROCESS USING NANOMOLDS	42
2.4 INSTRUMENTATION FOR DROP IMPACT EXPERIMENT	45
3. STATIC ROBUSTNESS.....	47
3.1 TRANSITION FROM THE CASSIE-BAXTER STATE TO THE WENZEL STATE	47
3.2 TWO FAILURE MECHANISMS	48

3.3	QUALITATIVE ANALYSIS	49
3.4	DERIVATION OF DIMENSIONLESS ROBUSTNESS PARAMETERS FOR MILLIHOODOOS .	54
3.5	QUANTITATIVE ANALYSIS.....	59
4.	SIMULATION OF STATIC WETTING PHENOMENA.....	61
4.1	HOODOO STRUCTURE	61
4.2	COMPARISON WITH EXPERIMENTAL RESULTS.....	68
4.3	APPLICATION OF THE SIMULATION MODEL AT THE NANOMETRIC SCALE.....	69
5.	DYNAMIC ROBUSTNESS	75
5.1	FAILURE MODES AND DYNAMIC SURFACE TENSION	78
5.2	BREAKTHROUGH PRESSURE FORMULA FOR A SQUARE ARRAY OF POSTS	79
5.3	WATER HAMMER PRESSURE	81
5.4	DROP IMPACT EXPERIMENT	83
6.	CONCLUSION	89
6.1	SUMMARY AND EVALUATION OF THESIS OBJECTIVES	89
6.2	FUTURE WORK	90
	APPENDIX	93
	BIBLIOGRAPHY	107

List of Figures

Figure 1.1 Lotus leaf (<i>Nelumbo Nucifera</i>).	16
Figure 1.2 Hydrophobic surfaces with various textures (SEM images) [16].....	16
Figure 1.3 (a) Hoodoo (b) microhoodoos and (c) omniphobic surface [28].....	18
Figure 1.4 Equilibrium contact angle (θ_E) and apparent contact angle (θ^*) [27].	19
Figure 1.5 Schematic illustration of the representative characteristic geometrical parameters in two different geometries [28]. (a) cross-sectional view of grates. (b) cross-sectional view of cylindrical fibers.	20
Figure 1.6 Various re-entrant structures in the literature [40, 41]. (a) mushroom structure. (b) metastable equilibrium state of high surface tension liquid ($\theta_E > 90^\circ$). (c) metastable equilibrium state of low surface tension liquid ($\theta_E < 90^\circ$). (d) The upper point indicates stable equilibrium ($\theta_E = \theta_0 > \theta$) and the lower point indicates unstable equilibrium for a low surface tension liquid ($\theta_E < 90^\circ$).	23
Figure 1.7 The texture angle (ψ) and direction of resultant force (F) by surface tension.	24
Figure 1.8 Non-wetting diagram [27, 42].	25
Figure 1.9 Calculation of areal Gibbs free energy density on a microhoodoo surface [27]. The global energy minimum is at the apparent contact angle of 74° (the Wenzel state, dark blue) while there is a local energy minimum at the apparent contact angle of 120° (the Cassie-Baxter state, light blue).....	26
Figure 1.10 Methanol evaporation experiment [28].	27
Figure 1.11 The illustration of the two failure modes and concept of nondimensionalization.....	28
Figure 1.12 The three and two dimensional computer graphic images of the Cassie-Baxter state (top) and Wenzel state (bottom) droplets based on lattice Boltzmann solution [47].	30
Figure 1.13 Distorted liquid-air interface supported by a square array of square posts [49].	31

Figure 1.14 Distorted liquid-air interface supported a square array of circular posts [50].	32
Figure 1.15 The application of opaque and transparent omniphobic surfaces.....	34
Figure 1.16 Plot of the robustness parameter (H^*) as a function of the spacing ratio (D^*) for droplets of octane (surface tension $\gamma_{lv}= 21.6$ mN/m) on various natural and artificial surfaces presented in the literature [27].....	36
Figure 2.1 Overview of the three steps for the three-dimensional printing (Connex500 TM).	40
Figure 2.2 Fabrication process for the nanomold.	43
Figure 2.3 Replica molding process for nanoposts.....	44
Figure 2.4 The SEM image of nanoposts.....	44
Figure 2.5 Measurement of apparent contact angle with water droplet on PFPE nanoposts.	45
Figure 2.6 Schematic view of beam splitter [68].....	45
Figure 2.7 Actual experiment setup using a beam splitter.	46
Figure 3.1 Three-dimensionally printed millihoodoos.	50
Figure 3.2 The Cassie-Baxter state droplet (top) and sequential images of two failure modes (bottom).....	50
Figure 3.3 Ethanol droplets with green dye on the textured surfaces with four card shapes shows the effect of negative minimum texture angles (ψ_{min}) on the two wetting regimes.	52
Figure 3.4 The overall results of millihoodoo experiment with theoretical prediction based on the dimensionless robustness parameters derived for microhoodoos.....	53
Figure 3.5 The scanning electron microscope (SEM) images and schematic oblique view of microhoodoos and millihoodoos. The upper illustration describes the unit area for the calculations of the dimensionless robustness parameters [28] and the lower illustration shows an important difference compared to the square hoodoos. The diagonal distance between the edge of two hoodoo cap parts is much greater than the horizontal or vertical distance between them (in case of top view).	55

Figure 3.6 The cross-sectional view of hoodoo geometry and some notations [28].	56
Figure 3.7 The overall results of millihoodoo experiment with theoretical prediction based on the generalized dimensionless robustness parameters. (a) standard hoodoo geometry. (b) re-entrant geometry with negative texture angle ($\psi = -90^\circ$) possessing the identical values of height (H) and spacing ($2D$).	60
Figure 4.1 The liquid-air-solid composite system including four millihoodoos.	62
Figure 4.2 Bottom facets for the millihoodoo model (red).	63
Figure 4.3 Pillar facets for the millihoodoo model (red).	64
Figure 4.4 Top facets for the millihoodoo model (blue and red).	66
Figure 4.5 Snapshot of the terminal window for Surface Evolver (Mac OS™ version).	67
Figure 4.6 The cross-sectional view of a droplet and millihoodoos (a snapshot in the middle of the calculation for an equilibrium state).	69
Figure 4.7 The oblique view of liquid-air-solid composite system including four nanohoodoos and a part of liquid-air interface.	70
Figure 4.8 Schematic overview of two failure mechanisms and criteria - the texture angle (ψ) and height of the lowest point of liquid (h).	71
Figure 4.9 Movie frames showing two kinds of failure mechanisms (nanohoodoo case).	72
Figure 4.10 Calculation of the texture angle (ψ) and height of the lowest point of liquid (h) with respect to pressure difference across the liquid-air interface of a millimetric droplet on nanohoodoos.	73
Figure 4.11 Increase in the robustness of Cassie-Baxter composite state on a nanohoodoo surface compared to a microhoodoo surface. The white scale bars in the three small images indicate 1mm.	74
Figure 5.1 Schematic drawing image of a square array of posts and SEM image of nanoposts made of PFPE.	75
Figure 5.2 Morphology of drop impact on a dry surface [51, 69].	76
Figure 5.3 Dynamic surface tension of water [70].	79

Figure 5.4 Two failure modes of the Cassie-Baxter state droplet on post structure.....	80
Figure 5.5 Sequential high-speed camera images of the drop impact on superhydrophobic surfaces with the impact velocity of 1.17m/s and the We of 19.0.....	85
Figure 5.6 Impact force vs. time at various impact velocities.....	86
Figure 6.1 Two approaches to achieve anti-reflection and self-cleaning – coating only (left) vs. micro/nanometric surface texture as well as coating (right) [74].	91

List of Tables

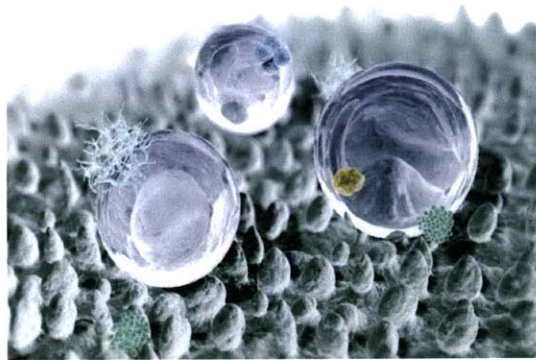
Table 5.1 Summary of the effect of each parameter on each of the six scenarios [51, 69]. R_a , R_w and θ_{rec} indicate the roughness amplitude, wave length, and wettability characteristic (receding angle), respectively.....	78
Table 5.2 Impact velocities and water hammer pressures.....	82
Table 5.3 Impact pressure at the peak impact force point at different impact velocities and on hydrophilic(HP) surface and superhydrophobic (SH) surface.....	88

Chapter 1

1. Introduction

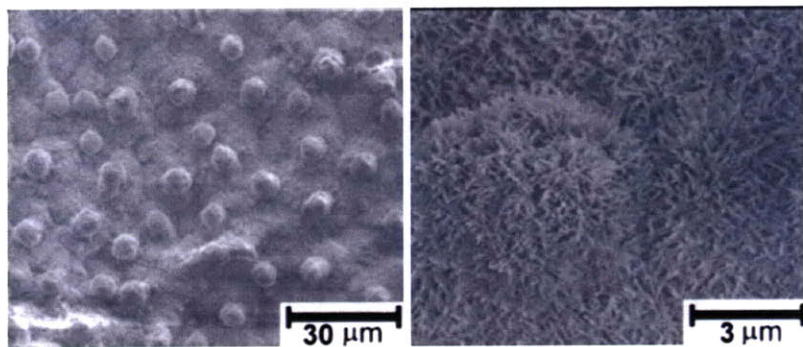
1.1 Motivation: hydrophobic and omniphobic surfaces

In the last decade, research on surfaces that are not wetted by water has attracted great interest [1-5]. A lotus leaf is a well-known example of a surface that is non-wettable with water, which is called a hydrophobic surface [4-7]. The water-repelling property of the lotus leaf is attributed two factors: surface chemistry and micro/nanometer-scaled surface structure [2, 8-11]. In addition, the dual-scaled structure has been focused and emphasized because this leads to an enhancement in its self-cleaning property, which has a broad range of applications (as shown in Section 1.3) [4, 5, 9, 12-15]. To mimic the hydrophobicity of natural examples many kinds of texture have been tested in the literature [9, 16-20]. A variety of materials from silicon to polymers as well as fabrication methods from Microelectromechanical Systems (MEMS) to replica molding process have allowed researchers to enhance the functionality of hydrophobic surfaces and to reduce manufacturing cost [12, 16, 21-24].



conservationreport.com/tag/nature/

(a) A computer graphic micrometric-scale image of three water droplets with contaminating particles on a lotus leaf.



(b) Scanning Electron Microscope (SEM) images of lotus leaf surfaces [25].

Figure 1.1 Lotus leaf (*Nelumbo Nucifera*).

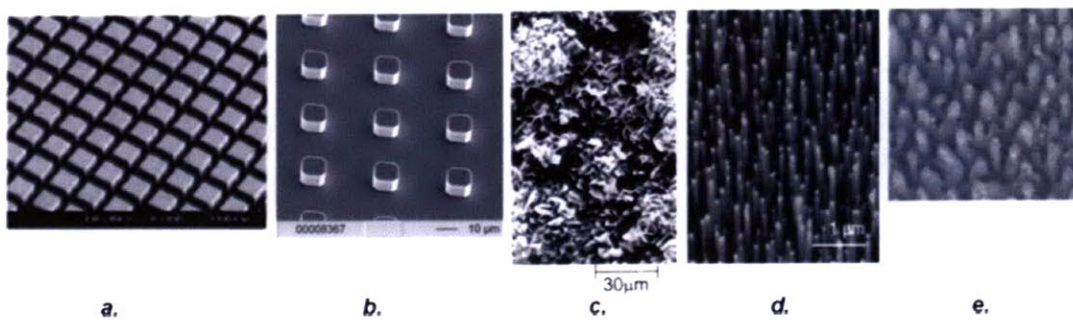


Figure 1.2 Hydrophobic surfaces with various textures (SEM images) [16].

The hydrophobic surfaces attain their non-wetting property by forming a solid-liquid-air composite interface when a liquid droplet is placed gently or when a droplet impacts on the solid surfaces. The composite state of droplets can be created because the textured surfaces trap plenty of small air pockets and the liquid droplets resides partially on the solid texture and partially on the trapped air; thus preventing the liquid from imbibing into the surface texture. (A more detailed explanation is given in the section 1.2.)

In addition to hydrophobic surfaces, many researchers and our group have developed the surfaces that are not wetted by a broad range of liquid and therefore named oleophobic or omniphobic surfaces [8, 26-30]. Whereas hydrophobic surfaces are easier to produce because of the higher surface tension (72 mN/m) of water, it has been difficult to achieve omniphobicity because many liquids including oils possess very low surface tension (e.g., for hexadecane , the surface tension is 27.5 mN/m). To overcome the limit of conventional textured surfaces, which provides equilibrium contact angles (θ_E) about 60 degrees at most with low surface tension liquids, a mushroom-like or nail-like re-entrant topography (similar to hoodoo in nature in Figure 1.3 (a)) was used [8, 30].

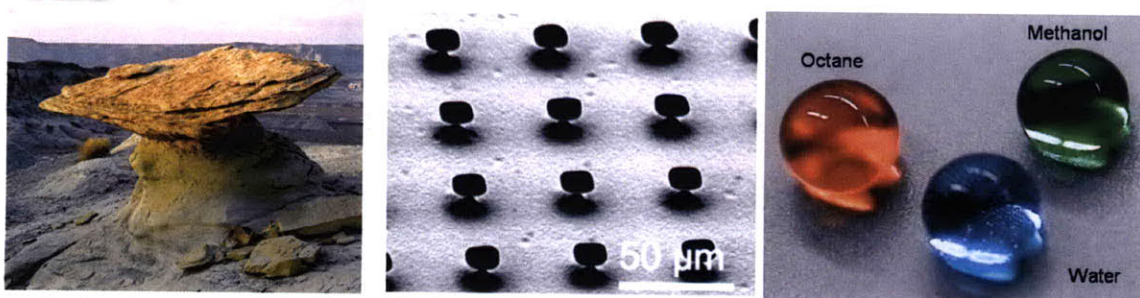


Figure 1.3 (a) Hoodoo (b) microhoodoos and (c) omniphobic surface [28].

1.2 Literature review

1.2.1 Equilibrium contact angle and apparent contact angle

To understand the mechanism that leads to sphere-like drop formation on hydrophobic and omniphobic surfaces, the Young's equation

$$\cos \theta_E = (\gamma_{sv} - \gamma_{sl})/\gamma_{lv} \quad (1.1)$$

should be first noted [31]. This relation illustrates the contact angle of liquids on chemically homogeneous smooth surfaces when the liquid-vapor-solid (denoted by l , v , and s , respectively) system is at an equilibrium state and it is also locally satisfied even on rough surfaces. The equilibrium contact angle is induced from the force balance among the three interfacial tensions (γ_{sv} , γ_{sl} , and γ_{lv}); therefore modifying any of the three tensions can change the local contact angle. The left illustration in Figure 1.4 is showing the equilibrium contact angle smaller than 90° . It is reported that the maximum equilibrium contact angle of water is nearly 120° on Teflon® surfaces [32]. In this work, we have used fluorodecyl polyhedral oligomeric silsesquioxane (POSS) as our surface

coating material to attain equilibrium contact angles such as 120° for water and 60° for ethanol [8].

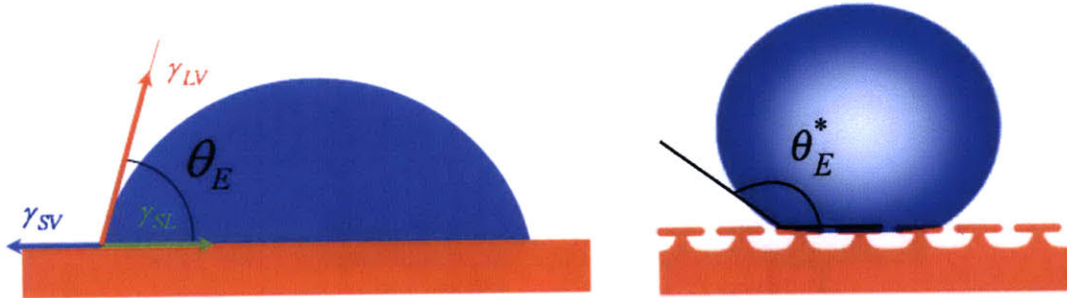


Figure 1.4 Equilibrium contact angle (θ_E) and apparent contact angle (θ^*) [27].

On textured surfaces there are two kinds of wetting state, leading to different apparent contact angles. First, liquid droplets can be partially supported by non-wettable air pockets entrapped between solid asperities much smaller than the size of droplets. In this case, an apparent contact angle (θ^*) is given by the Cassie-Baxter relation

$$\cos \theta^* = r_\phi \phi_s \cos \theta_E + \phi_s - 1 \quad [33]. \quad (1.2)$$

Here r_ϕ is the roughness of the wetted surface, ϕ_s is the area fraction of the liquid-air interface occluded by the surface texture (See Figure 1.5), and θ_E is the equilibrium contact angle on a smooth surface of the same chemistry as the textured surfaces, given by Young's equation.

On the other hand, there is another wetting regime in which the space between textured solid structures underneath droplets is fully-wetted with liquids. The apparent contact angle in the fully-wetted Wenzel state is given by the Wenzel relation

$$\cos \theta^* = r \cos \theta_E \quad (1.3)$$

where r is the surface roughness [34]. As shown in Figure 1.5, r is represented as green line and clearly greater than unity if a surface is not flat.

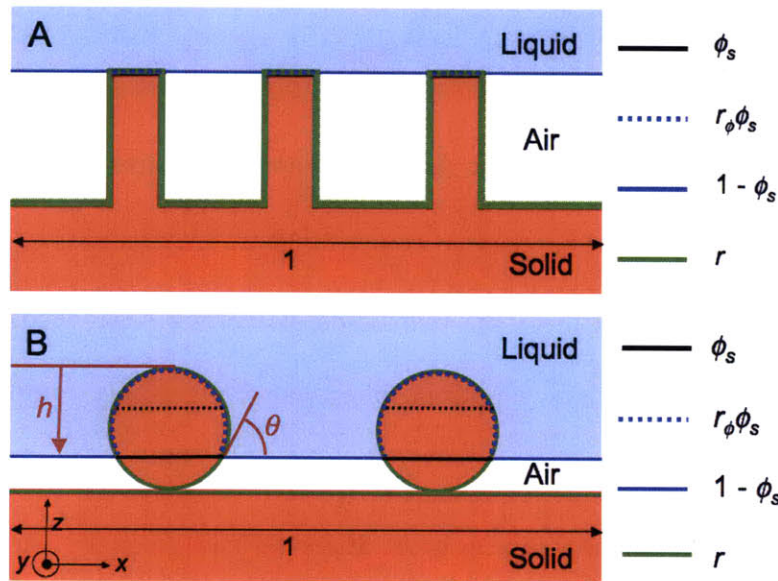


Figure 1.5 Schematic illustration of the representative characteristic geometrical parameters in two different geometries [28]. (a) cross-sectional view of grates. (b) cross-sectional view of cylindrical fibers.

For high surface tension liquids including water, a square arrays of posts coated with low surface energy material have been widely used to design superhydrophobic surfaces, leading to $\theta^* > 150^\circ$ and low contact angle hysteresis i.e., the difference between the apparent advancing contact angle and apparent receding contact angle [2,

9]. As shown in the Cassie-Baxter relation, for post-textured surfaces where $\phi_s (= r_\phi \phi_s)$ is smaller than unity, when $\theta_E > 90^\circ$ the apparent contact angle can be maximized greater than 150° . The high apparent contact angle can also be obtained from the Wenzel relation if $\theta_E > 90^\circ$ and $r > 1$. However, it is hard to achieve a low contact angle hysteresis because liquid fill the space between asperities and tends to be pinned on rough surfaces ($r > 1$), whereas a Cassie-Baxter state droplet has a tendency to weakly adhere to the small wetted portion of rough solid surface [2, 10]. An array of posts, if designed to have small spacing and great height enough to prevent the imbibition of water between the posts, can support composite interfaces in case of water droplets. On the contrary, low surface tension liquids always wet this texture, as the Young equation cannot be satisfied at any location on an array of posts for such liquids because the direction of force due to the surface tension is downward, leading to the complete wetting regime. Therefore, a surface on which the local force balance can be satisfied is necessary for the existence of composite interfaces.

1.2.2 Re-entrant structure

The re-entrant structure refers to a surface topography that has continuously varying texture angle ψ as shown in Figure 1.7, i.e., the angle between the horizontal line and the tangential line at the liquid-air-solid three phase contact line, greater and less than 90° . The cross-section of a cylindrical fiber is a representative example of this

re-entrant structure. Natural hoodoo structure (Figure 1.3) is another example of the re-entrant structure that has the texture angle from 0° to 180° .

Many researchers have focused similar kind of surface texture for the development of high apparent contact angles with low surface tension liquids [35-39]. Nosonovsky has first studied the stability of equilibrium state of flat liquid-air interface on a multiple re-entrant structure for liquids with the low equilibrium contact angles (Figure 1.6) [40]. He demonstrated interfacial energy analysis that the liquid-air interface can be suspended by two and three-dimensional pillars with semicircular bumps and grooves. Marmur also illustrated the re-entrant structure similar to hoodoo structure as shown in the Figure 1.6 (a), (b), and (c) [41]. He showed through rigorous mathematical approach that it is possible to achieve a high apparent contact angle from a low equilibrium contact angle if the surface topography is re-entrant. Their ideas are summarized in Figure 1.6. In conclusion, the local force balance is satisfied when $\theta_E = \psi$ and therefore there is a possibility that a solid-liquid-air composite interface might exist at such a location.

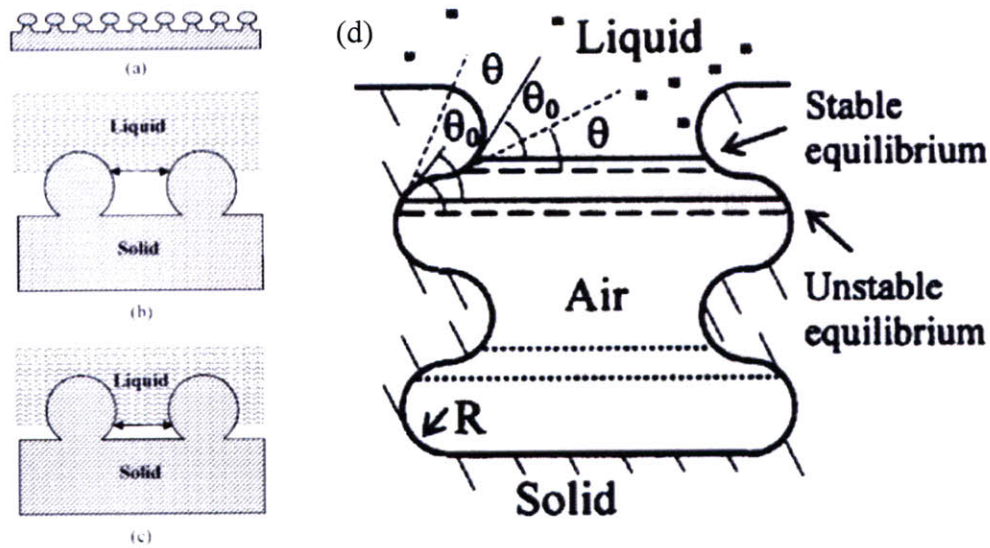


Figure 1.6 Various re-entrant structures in the literature [40, 41]. (a) mushroom structure. (b) metastable equilibrium state of high surface tension liquid ($\theta_E > 90^\circ$). (c) metastable equilibrium state of low surface tension liquid ($\theta_E < 90^\circ$). (d) The upper point indicates stable equilibrium ($\theta_E = \theta_0 > \theta$) and the lower point indicates unstable equilibrium for a low surface tension liquid ($\theta_E < 90^\circ$).

If $\theta_E - \psi > 0$, the direction of force generated by surface tension is upward and this hoodoo structure can balance with pressure difference across the liquid-air interface. Thus the value of ψ smaller than the equilibrium contact angle enables this hoodoo structure to support low surface tension liquid, which has low equilibrium contact angle (See Figure 1.4) on flat and smooth surfaces homogeneously coated with low surface energy material.

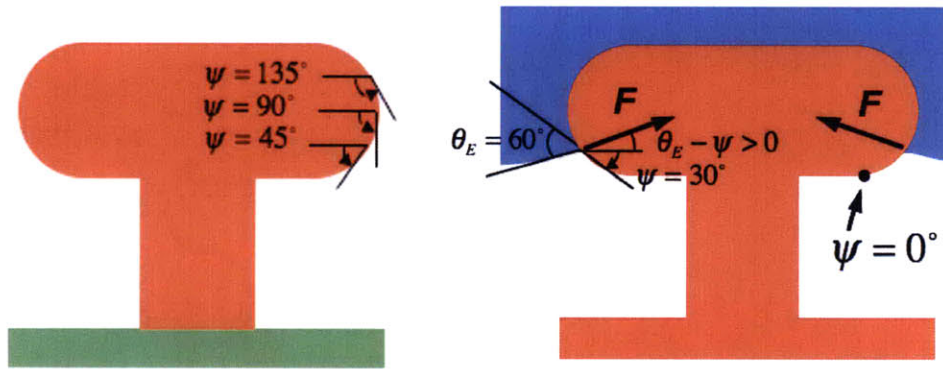


Figure 1.7 The texture angle (ψ) and direction of resultant force (F) by surface tension.

1.2.3 Thermodynamics - metastable composite state

As demonstrated in the previous section, the Cassie-Baxter (CB) composite state is the only way to attain both high apparent contact angles and low contact angle hysteresis for all kinds of liquids. However, calculations show that the CB composite state is local minimum in the free energy and metastable for low surface tension liquids (red dot line in Figure 1.8) whereas the fully-wetted state represents global minimum (blue solid line in Figure 1.8) [27].

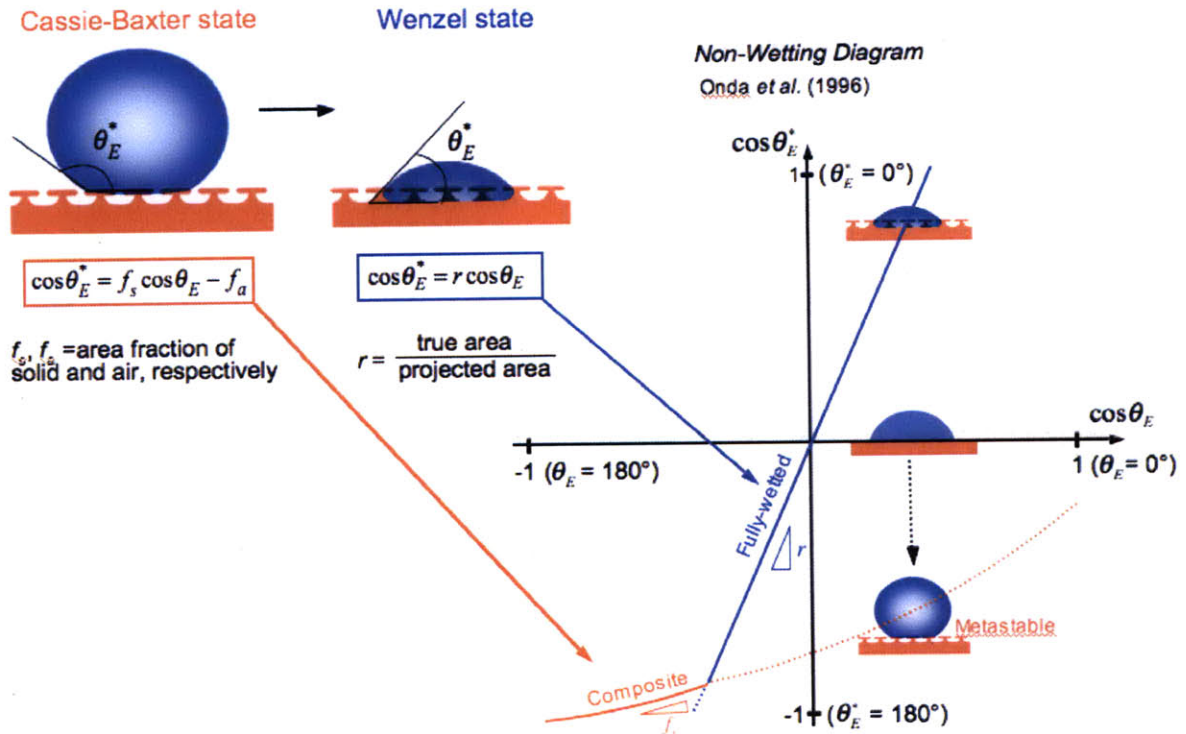


Figure 1.8 Non-wetting diagram [27, 42].

Tuteja *et al.* have calculated the areal Gibbs free energy density as a function of apparent contact angle and dimensionless height (h/z_{max}) on an omniphobic microhoodoo surface and results are shown in the Figure 1.9. Here G^*_{min} is the areal Gibbs free energy density for the composite interface. The two minima in Figure 1.9 at $h/z_{max} \sim 0.05$ and $h/z_{max} \sim 1$ correspond to a metastable composite (local minimum) and a fully wetted (global minimum) interfaces, respectively. The inset shows a schematic of the solid substrate. The discontinuity in the y -axis (h/z_{max}) is for easier visualization of the minimum in free energy corresponding to the composite interface based on the thickness of the hoodoo caps ($2R = 0.3 \mu\text{m}$) and height of the hoodoos ($H = 7 \mu\text{m}$).

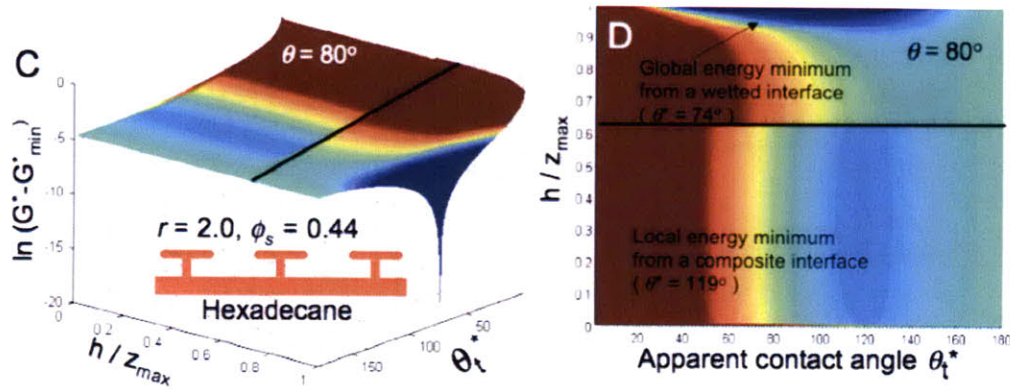


Figure 1.9 Calculation of areal Gibbs free energy density on a microhooedoo surface [27]. The global energy minimum is at the apparent contact angle of 74° (the Wenzel state, dark blue) while there is a local energy minimum at the apparent contact angle of 120° (the Cassie-Baxter state, light blue).

1.2.4 Robustness of the composite state

From the free energy calculation, Tuteja *et al.* argued that the transition from the Cassie-Baxter composite state to the Wenzel fully-wetted state is induced when the pressure difference between the liquid and air increases up to a critical value defined as the breakthrough pressure, i.e., the maximum pressure difference that the liquid-air interface can resist, by the curvature of liquid droplet or other external perturbations, which is similar to many studies on the transition [43-46]. This robustness problem was demonstrated by methanol evaporation experiment in Figure 1.10. The equilibrium shape of a liquid droplet is nearly spherical because it is governed by the balance between the gravity and surface tension ($R_{\text{drop}} \sim \ell_{\text{cap}}$). As the droplet size decreases by evaporation,

the pressure difference given by the Laplace equation i.e., $\Delta P(t) \approx P_{Laplace} = 2\gamma_{LV} / R_{drop}(t)$ increases. When the pressure difference reaches the critical breakthrough pressure by the evaporation, the Cassie-Baxter state transitions to the Wenzel state.

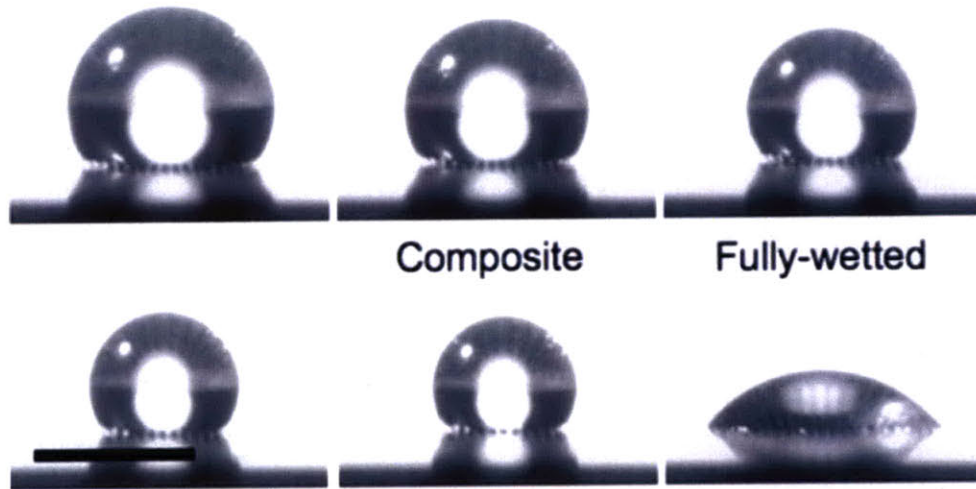


Figure 1.10 Methanol evaporation experiment [28].

Although the calculated energy surfaces in Figure 1.9 were approximating the flat liquid-air interfaces, Tuteja *et al.* hypothesized more realistic description has a curvature because of the pressure difference at the interface between the liquid and air. Based on this distorted liquid-air interface shape (Figure 1.11), they identified then two different kinds of failures on re-entrant structure, illustrated in Figure 1.9.

When the droplet approaches the hoodoo cap parts (i.e., the top round disk parts on the pillars), the lowest point of the liquid-air interface touches the bottom of solid between the hoodoos just before the other parts of the interface reach the hoodoo cap

parts. Once the contact occurs, it leads to a spontaneous wetting on the solid surface (the left image in Figure 1.11).

The second case is when the height of hoodoos is great enough to prevent the first failure mechanism. The composite contact line (i.e., the two point where the liquid (blue), air (white), and solid (red) contact in Figure 1.11) first reaches the point of the minimum texture angle (ψ_{\min}) before the lowest part of liquid-air interface wets the bottom solid surface. This case leads to another instantaneous wetting from the point of the minimum texture angle because the curvature of liquid-air interface cannot resist a greater pressure difference across the interface and instead advances across the surface from point A towards point B. (the right image of Figure 1.11)

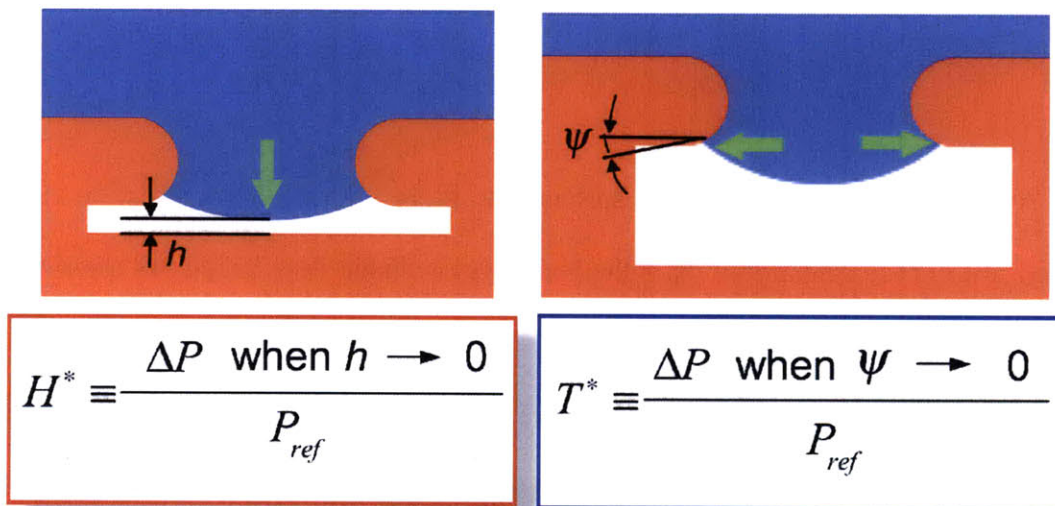


Figure 1.11 The illustration of the two failure modes and concept of nondimensionalization.

For the evaluation of robust omniphobic surface structures, Tuteja *et al.* developed suitable dimensionless criteria that assess the robustness of the composite state and the two kinds of failure modes. The two dimensionless design parameters robustness height (H^*) and robustness angle (T^*) are the ratio between the breakthrough pressure in two failure modes and the minimum reference pressure of a millimetric droplet ($P_{ref} = 2\gamma_{lv}/\ell_{cap}$), where $\ell_{cap} (= \sqrt{\gamma_{lv}/\rho g})$ is the capillary length, γ_{lv} is the surface tension and ρ is the density of the liquid.

The value of dimensionless robustness parameters can be interpreted as follows. It is obvious that the value of unity represents the balance between the actual pressure resistance of the textured surface and the reference pressure; thereby if the values of H^* and T^* are greater than unity, the textured surface can support the composite interface under pressure difference greater than the reference pressure. The surface is referred to be robust against perturbations. On the other hand, the lower value of either H^* or T^* than unity is interpreted as low inherent robustness of the textured surface. In summary, the greater the values of both dimensionless design parameters are, the more robust the textured surface is.

As well as the evaluation for the robustness of liquid-air-solid composite interface on present surface texture, these dimensionless parameters provide a guideline on how to obtain or optimize the robustness of omniphobicity by designing the dimensions of the surface features. More detailed information is covered in the next section 1.3 on the objectives of this work as well as in Chapter 3 and 4.

1.2.5 Numerical calculations of breakthrough pressure

In this section, we provide an overview of the recent work in the numerical calculation for breakthrough pressure on various textured surfaces. Most of these calculations studied the shape of liquid-air interface under pressure difference across it, on a square array of pillars with flat top surfaces. Dupuis and Yeomans developed a dynamic model that presents a liquid droplet on an array of micrometer-scale posts using a lattice Boltzmann solution of the governing equation of a spreading droplet [47, 48]. This model provided an apparent contact angle from the three-dimensional shape of the droplet and demonstrated the effect of topologically patterned substrate. Further, by imposing the gravitational field on the model, it showed a clear transition from the Cassie-Baxter state to the Wenzel state.

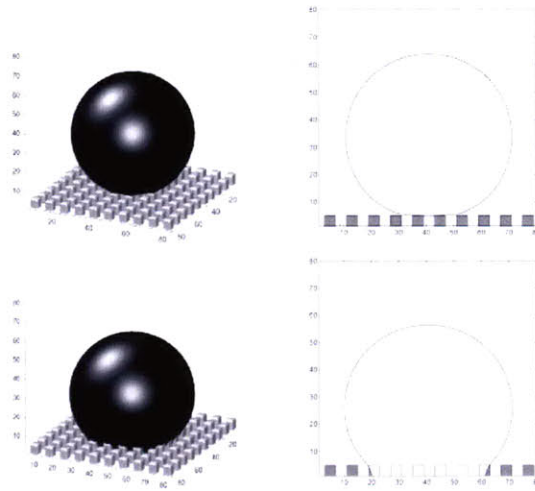


Figure 1.12 The three and two dimensional computer graphic images of the Cassie-Baxter state (top) and Wenzel state (bottom) droplets based on lattice Boltzmann solution [47].

Zheng *et al.* intensively studied the role of the pressure difference across the water-air interface and calculated the maximum sustainable pressure (i.e., breakthrough pressure) [49]. They approached the pressure and transition problems by considering the effect of each sharp edge on square posts. This numerical calculation revealed the optimal dimensions of square arrays of post (i.e., a , b , and H in Figure 1.13) for a possible high pressure difference above 10^5 Pa, for example rain drop impact pressure.

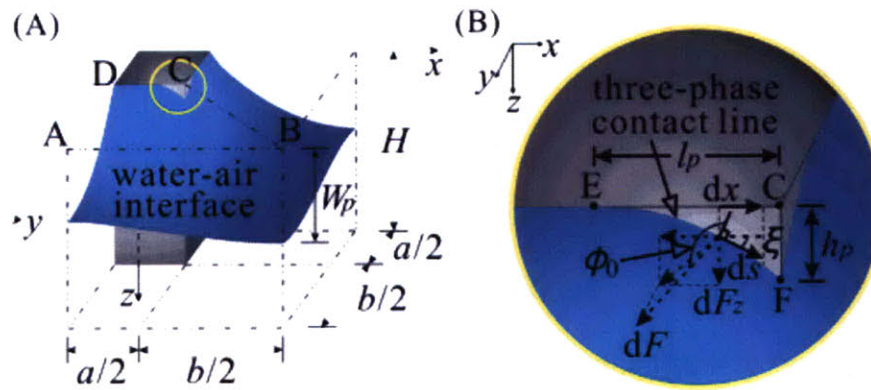


Figure 1.13 Distorted liquid-air interface supported by a square array of square posts [49].

Lobaton and Salamon computed the shape of liquid-air interface of a pressurized fluid on various cap-shaped posts including re-entrant structure [50]. Their simulation model was based on the Young-Laplace equation and an overall force balance between the surface tension and pressure difference. They also compared their prediction using the numerical model with many previous experimental results containing direct measurement of the distorted liquid-air interface as well as the critical pressure and dimensions of posts

inducing transition from the Cassie-Baxter state to the Wenzel state, which was in a good agreement with the reported experiment results.



Figure 1.14 Distorted liquid-air interface supported a square array of circular posts [50].

1.2.6 Drop impact pressure

Apart from the static or quasi-static droplet on a non-wettable surface, the interaction between dynamic droplets and textured surfaces is important for a wide range of practical application because the impact of droplets with high velocity on solid surfaces generates much higher pressure, leading to an irreversible transition between the two wetting regimes on the textured surfaces.

The drop impact pressure was first highlighted because of the importance of erosion problem due to the drop impact and has been an interesting research field for about one century [51, 52]. Engel first estimated the impact pressure when a water drop collides with solid surfaces based on the analysis of sequential high-speed camera images of the drop collision [53, 54]. He derived the formula that quantifies the water hammer pressure ($P_{WH} = \alpha \rho c v$, where α is a coefficient determined by experiment, ρ is the density of the working liquid, c is the velocity of sound in the liquid, and v is the

impact velocity), i.e., the maximum pressure during the impact, under several assumptions based on the observation using a high-speed camera. He considered the effect of pressure wave propagation inside the water drop after the contact instant and added that the coefficient α is about 0.2 if the impact velocity of water drop is around 9 m/s.

Nearing *et al.* measured the impact force and impact pressure by the collision between water drop and solid surfaces using piezoelectric pressure sensor [55, 56]. They compared the experimental data with Engel's theory and reported that the coefficient α in the water hammer pressure equation is approximately 0.1 at around the impact velocity of 10 m/s.

More recently, Deng, Varanasi and coworkers applied the concept of water hammer pressure to the robustness of the Cassie-Baxter state on various textured surfaces [57]. They categorized the motion of water droplets after impact into three cases by comparing the water hammer pressure with Bernoulli and capillary pressures. For example, if the characteristic pressure of the textured surface is greater than the water hammer pressure, the droplet completely bounces off the solid surface. They interpreted this rebound stems from the inherent property of the designed textured surface that induces the high robustness of the composite state.

1.3 Applications and robustness problems

Non-wettable solid surfaces with various kinds of liquids have been highlighted in

many studies for a wide range of practical applications including smart fabric, engine elements, and turbine blades [58-60]. Non-wettability is a useful property in the combat uniform industry because a fabric with omniphobicity can inhibit the infiltration of harmful chemicals into soldier's skin.

In addition, due to the high apparent contact angles and low hysteresis of liquids on the superhydrophobic surfaces, they possess an inherent self-cleaning property, which can reduce an enormous amount of cost in cleaning private and industrial surfaces. Finally, liquid drag reduction for ships or submarines or icephobicity for airplanes attracts many researchers by opening a pathway to use the superhydrophobicity on textured surfaces [61-64]. In the near future, the integration between interfacial fluid mechanics and optics would be necessary for many applications including display panels of electronics.



defense-technologynews.blogspot.com apple.com

Figure 1.15 The application of opaque and transparent omniphobic surfaces.

Despite of attractive features including self-cleaning property, the artificial hydrophobic and omniphobic surfaces have a limit in terms of ability to maintain the high apparent contact angles against pressure difference across the liquid-air interface.

This substantial problem has initiated a discussion of the robustness of non-wetting states. As shown in Fig. 1.6, the size of a liquid droplet decreases as it evaporates and then abruptly transitioned into the Wenzel state that shows low apparent contact angle. Laplace pressure increases as the radius of the droplet decreases and finally surface tension of liquid at the contact line cannot balance with the critical pressure difference beyond a threshold. In addition, dynamic droplets have much higher pressure difference depending on impact velocity and physicochemical properties of liquids [57, 65].

In particular, typical micrometric post or hoodoo surfaces can support breakthrough pressure on the order of 100 Pa, which is much lower compared to pressure differences experienced in our daily life. The static pressure under 1 meter of water is about 10 kPa and the impact pressure of raindrops (1m/s) is approximately 200kPa. More robust non-wettable surfaces are required for practical application.

1.4 Objectives and approach

The goal of this thesis is to explore various topics relevant to the robustness of omniphobicity to overcome the critical practical problems associated with the breakthrough pressure. The main topics in this work is based on the systematic analysis of the robustness in the Figure 1.16, which shows the effect of multiple length scale on the robustness.

Based on this design framework, at first re-entrant structure at the millimetric scale was investigated using a new fabrication method, three-dimensional printing. The

two failure mechanisms and robustness of static liquid droplet on the millihoodoo structure were examined experimentally and then simulation models describing the composite system at the multiple length scales were verified using the experiment results. Exploiting the *a priori* evaluation method, the breakthrough pressure of nanopost was calculated and correlated with the impact force of dynamic droplets.

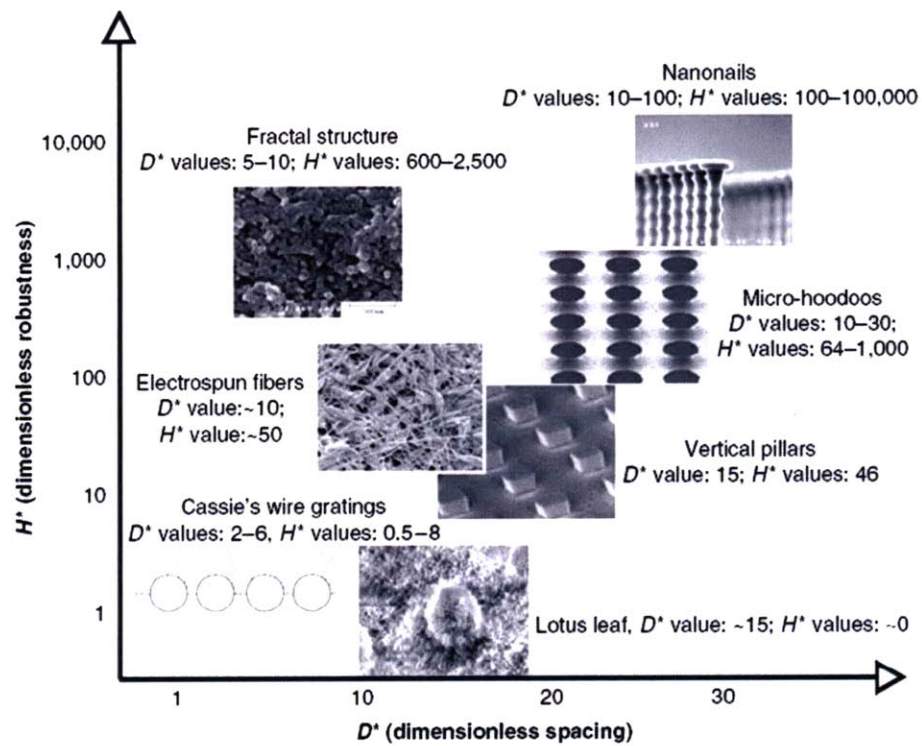


Figure 1.16 Plot of the robustness parameter (H^*) as a function of the spacing ratio (D^*) for droplets of octane (surface tension $\gamma_{lv} = 21.6$ mN/m) on various natural and artificial surfaces presented in the literature [27].

1.5 Chapter description

Before the three main approaches and results in this work, the methodology that will be used in the three chapters is first introduced. Chapter 2 describes three-dimensional printing and dip-coating for the fabrication of millimetric hoodoos, Surface Evolver for the development of simulation models for the droplet-air-texture composite system, and replica molding process for the fabrication of nanometric posts. In addition, instrumentation that was employed to investigate the dynamic robustness of composite system is added.

In Chapter 3, based on the discussion of free energy and pressure difference across the liquid-air interfaces introduced in Chapter 1, we primarily delve into the transition from the Wenzel state into the Cassie-Baxter state using millimetric textured surfaces. The effects of the dimensionless robust design parameters for re-entrant geometry on distorted interfaces and the two failure modes are extensively explored with ethanol evaporation experiment on millihoodoo surfaces.

In Chapter 4, with the basis of the experimental results in Chapter 3 and other literature, an *a priori* method that evaluates the robustness of the Cassie-Baxter state at the multiple texture scales was developed using simulation software Surface Evolver. Further, the input routines modeling the liquid-air-solid composite system were used to compute the shape of evaporating ethanol droplets on omniphobic surfaces, varying the volume of liquid droplets. At the end of the chapter, changes in the distorted liquid-air interface of droplets on nanohoodoo surfaces were also realized altering the pressure

difference across the interface directly and exploited to predict the breakthrough pressure of the nanohoodoo surfaces.

In Chapter 5, to explore the robustness of liquid droplets that dynamically interact with textured surfaces, a water drop impact experiment was conducted using transparent superhydrophobic nanopost surfaces. In addition to the observation of side and bottom view utilizing a beam splitter, the impact force was measured using a piezoelectric film to compare it with the water hammer pressure at the impact velocity ranging from 0.5 m/s to 2 m/s.

In Chapter 6, three main works – millihoodoo, Surface Evolver modeling, and nanopost- are summarized with the evaluation of thesis objectives in each chapter. Finally, future work associated with the combination between the robustness issue in wetting and the transparency issue in optics is suggested.

Chapter 2

2. Methodology

This section is devoted to the introduction of various fabrication methods, computer simulation software, and instrumentation that were used for the work in the subsequent chapters. Chapter 3 contains a description of the three-dimensional printing and dip coating protocols used to prepare textured surfaces. In Chapter 4, the finite element method (FEM) based simulation software Surface Evolver is introduced to provide an overview of the background principles that were optimized to model interfacial phenomena. Finally, the replica molding process used to fabricate polymer-based transparent superhydrophobic surfaces is detailed in Chapter 5.

2.1 Fabrication of millihoodoos

2.1.1 Three-dimensional printing

Millihoodoos were fabricated using a three-dimensional printer (Connex500TM, Objet). Conventional Microelectromechanical Systems (MEMS) technology was not utilized, as MEMS techniques focus on the fabrication of submillimetric features,

whereas our target is in the range of several millimeters. The steps for the three-dimensional printing are shown in Figure 2.1.

First, surface structure design files were created and transformed into the stereolithography (.stl) file format using SolidWorks™. Based on the three-dimensional structure information in the design (.stl) file, the Connex500™ printed ultraviolet (UV)-curable polymer drops on the horizontal plane. The volume of each drop is approximately 25 pL including supporting material. Then the printer cured the printed drops by exposing them to UV light, layer by layer. After finishing printing, the sample with supporting material was soaked in sodium hydroxide solution (2 wt%) for 10 minutes to facilitate removal of the supporting material using a water-jet and was then brushed.

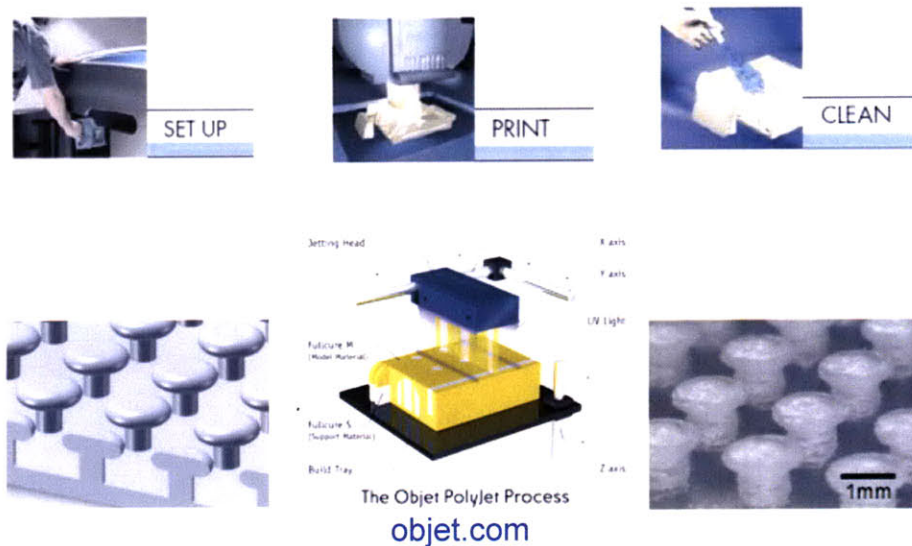


Figure 2.1 Overview of the three steps for the three-dimensional printing (Connex500™).

There are some important points to consider for the design of the structure along with the dimensionless robustness parameters introduced in the Chapter 1. First, the position of each printed drop is digitalized because of the minimum volume (25 pL \sim $42 \times 42 \times 16 \mu\text{m}^3$) of UV-curable polymer drops. Second, relatively poor accuracy, i.e., the distance between two printed drops in different layers that are designed to be at the vertically identical place ($\sim 100 \mu\text{m}$), compared to the resolution (600 dpi from the minimum droplet size of $42 \mu\text{m} \times 42 \mu\text{m}$ on the horizontal plane) influences the dimension of actual printed structures. The dimensions of printed samples were examined using a scanning electron microscope (SEM) (following dip-coating, as explained in the following section) and then averaged.

2.1.2 Dip Coating

To decrease the surface energy of the solid textured surface, the three-dimensional printed samples were coated with a nanocomposite comprised of 50 wt% fluorodecyl POSS (polyhedral oligomeric silsesquioxane) and 50 wt% Tecnoflon (BR9151). The Tecnoflon and fluorodecyl POSS were dissolved in Asahiklin AK-225 (Asahi glass company) at an overall solids concentration of 10mg/ml, the printed substrates were submerged in the solution for 2 minutes at room temperature, and the dip-coated samples were then dried in a vacuum oven for 30 minutes at 60°C [8].

2.2 Surface Evolver

Surface Evolver is a C language-based simulation program that has been developed by Brakke to calculate the free energy state of a system on the basis of a mean curvature theory [66, 67]. The steps for calculating the equilibrium shape of the liquid-air interface of droplets are as follows. Physico-chemical conditions are specified, including the surface geometry that is composed of vertices, edges, facets, and bodies, and Surface Evolver divides facets and triangulates them. According to the given parameters, such as surface tension, contact angle, density, volume of liquids and gravitational field, the triangles evolve and move to another location to satisfy the force balance and minimize the free energy of the liquid-air-solid composite system. Other external forces, such as external pressure, can also be applied in calculating an equilibrium state using the mean curvature theory.

The physico-chemical conditions are coded and transferred into the “evolver” by an input routine, which is written by users. For more detailed information about the Surface Evolver and the composition of an input routine used in this work, see the general manual written by Brakke and Chapter 4 in this thesis.

2.3 Replication process using nanomolds

To produce rough hydrophobic surfaces similar to the micro bumps on lotus leaf, nanomolds were first prepared using conventional Microelectromechanical Systems

(MEMS) techniques. A mask was designed with a nanopattern comprised of a square array of small holes (diameter ~ 500 nm). This pattern was transferred onto a photoresist (PR)-coated standard 6 in silicon wafer utilizing conventional stepper-photolithography technology (Nikon NSR2005i9TM). Then the silicon wafer was etched anisotropically using the developed photoresist pattern as an etching mask (by Applied Materials P5000 Mark II EtcherTM).

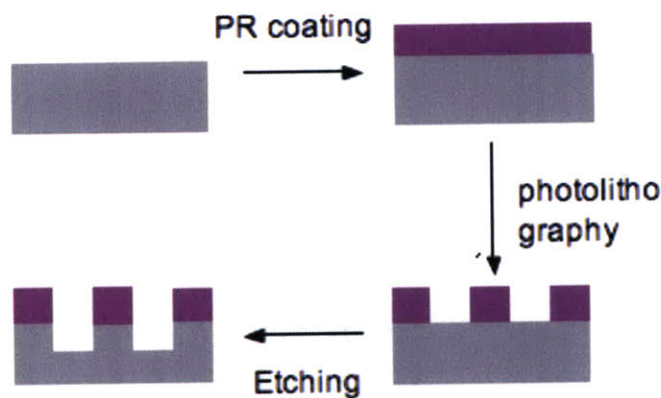


Figure 2.2 Fabrication process for the nanomold.

The perfluoropolyether (PFPE) replica molding process used for the preparation of textured polymeric substrates is summarized in Figure 2.3 (in collaboration with Dr. Adam Meuler in the department of Chemical Engineering at Massachusetts Institute of Technology (MIT)). The PFPE oligomers were poured onto the nanomold and then cured by exposing them to ultraviolet radiation (wavelength $\lambda = 365$ nm). The cured post structure (Figure 2.4) was then peeled off the mold.

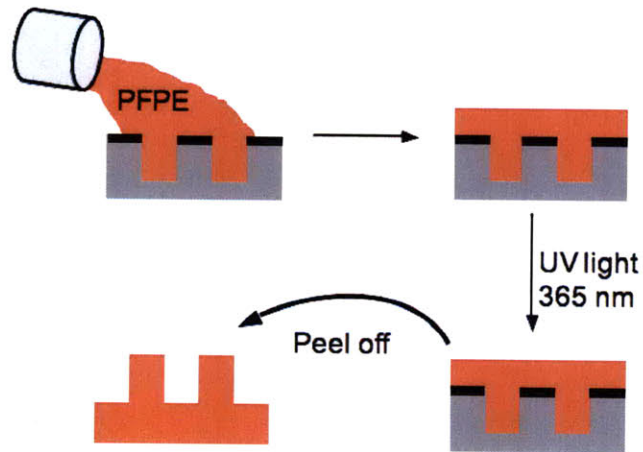


Figure 2.3 Replica molding process for nanoposts.

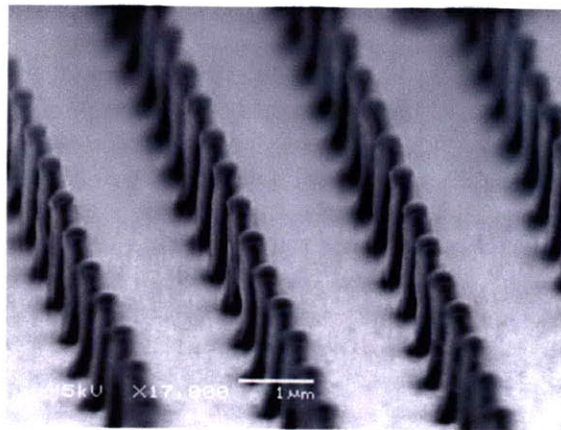


Figure 2.4 The SEM image of nanoposts.

This textured PFPE surface provided low solid surface energy leading to high equilibrium and apparent contact angles (Figure 2.5) for water. In addition, sufficient optical transparency was attained to capture both front and bottom views using a beam splitter as illustrated in Figure 2.6.

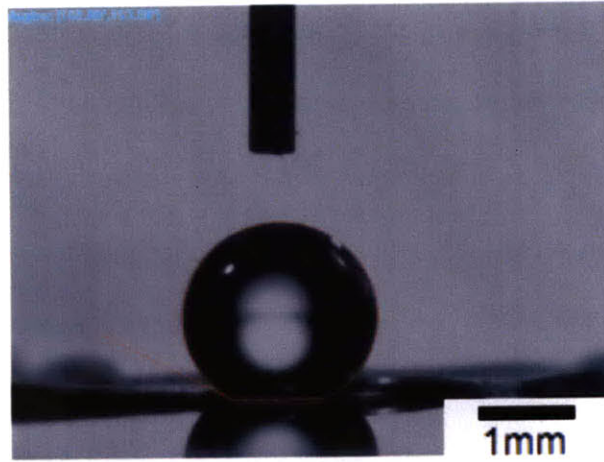


Figure 2.5 Measurement of apparent contact angle with water droplet on PFPE nanoposts.

2.4 Instrumentation for drop impact experiment

In Chapter 5, a drop impact experiment designed to investigate the dynamic aspect of the robustness of the Cassie-Baxter state droplet is described. The schematic overview and actual instrument setup for the experiment are provided in Figures 2.6 and 2.7. A beam splitter was used to enable simultaneous viewing of both the side and bottom of liquid droplets, as illustrated in Figure 2.6.

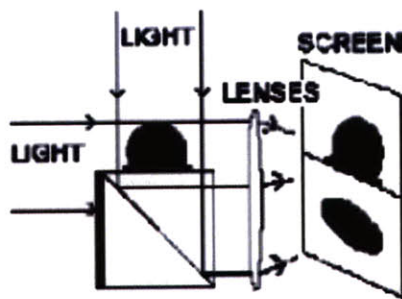


Figure 2.6 Schematic view of beam splitter [68].

A photograph of the actual instrument setup comprised of a light emission diode (LED), another light source, a beam splitter, and a syringe is provided in Figure 2.7. A series of drop impact images were obtained using a Phantom V5.0TM high-speed camera (5000 frames per second). The impact force was measured using a piezoelectric film connected to the universal serial bus (USB) data acquisition (DAQ) device and then analyzed using LabVIEWTM.

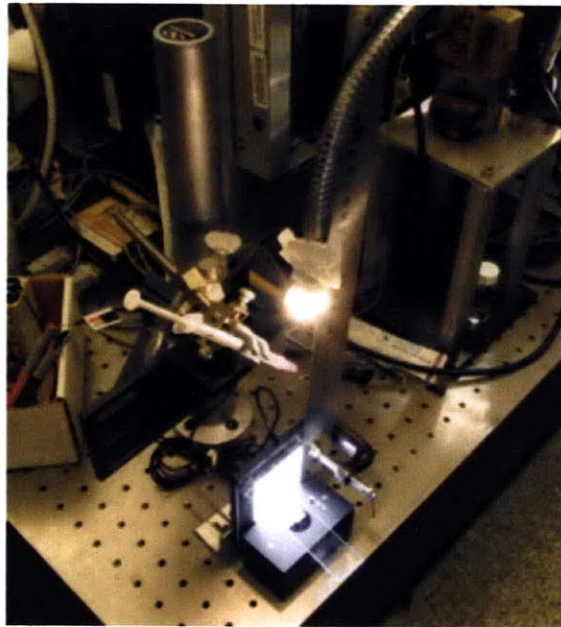


Figure 2.7 Actual experiment setup using a beam splitter.

Chapter 3

3. Static Robustness

Our interests were to image bulging interfaces and to explore gradual transition to failure by using commercial camera. These interests motivated us to fabricate hoodoo geometry on the millimeter scale and to use ethanol as the working liquid. Ethanol not only evaporates quickly but has a surface tension as low as decane; therefore, we reduced our experiment time to record the gradual transition of low surface tension liquid droplets as pressure difference increased, i.e., ethanol droplets evaporated isothermally.

3.1 Transition from the Cassie-Baxter state to the Wenzel state

As explained in the literature review section in Chapter 1 Introduction, the transition of a liquid droplet in the Cassie-Baxter state to the Wenzel state stems from the metastability of the Cassie-Baxter state in the specific region where the red dot line is in Figure 1.8 [42]. In this region, thermodynamically, the Wenzel fully-wetted state is the global minimum energy state and the Cassie-Baxter composite state may possess

several local minimum energy states. When the energy barrier originated from solid surface topography is overcome by some external perturbations, such as evaporation of the liquid, vibration, and impact by dynamic droplets, the Cassie-Baxter state transitions into the Wenzel state and the liquid-air-solid composite system is stabilized. As a consequence of this transition, the apparent contact angle generally decreases whereas the equilibrium contact angle is satisfied locally at the composite contact line. In this chapter, we first review the dimensionless robustness parameter and the meaning of the two failure mechanisms. Qualitative and quantitative analyses are then followed with the experimental results using the three-dimensionally printed re-entrant structures.

3.2 Two failure mechanisms

It is assumed that there are two kinds of the transition of a composite state liquid droplet. The first category is when the lowest part of the distorted liquid-air interface touches the bottom of the solid between two asperities because of the pressure difference across the liquid-air interface. The second case is when the height (or aspect ratio defined as the ratio between height and spacing) of asperities is large enough to prevent the liquid-air interface from reaching the bottom first. In this case, the three-phase contact line approaches the point of the minimum texture angle (ψ_{\min}) as the pressure difference increases, before the first case occurs. As the composite contact line reaches the minimum texture angle point, thermodynamics indicates that the state of the composite system passes on the summit of energy barrier. The next step is spontaneous

imbibition into the asperities, which is similar to the first case. However, these two mechanisms have not been verified by using video camera due to the limit of the size of the surface texture.

3.3 Qualitative analysis

One of the most significant component of this work is to show the transition directly through a video camera. To allow to video the transition, millimetric scale is employed because the value of dimensionless robustness parameters H^* and T^* is about unity at this scale, which means it is close to the transition point of millimetric liquid droplets. Moreover, the observation problem relevant to small texture scale of micro-textured surfaces can be avoided because the texture scale is large enough to video using a video camera.

To determine the specific dimension of the hoodoo structure at the millimetric scale, the dimensionless robustness parameter that was derived in the PNAS paper has played a key role. Some candidate designs that are distributed like a square array on the H^* and T^* graph around the $H^*=T^*=1$ were tested, as shown in the Figure 3.1. The state of liquid droplets was checked by gently placing droplets on each design and then two approaches were employed: decreasing the height of hoodoo and increasing the spacing between neighboring hoodoos. The former led to the H^* failure mode and the latter caused the T^* failure mode.

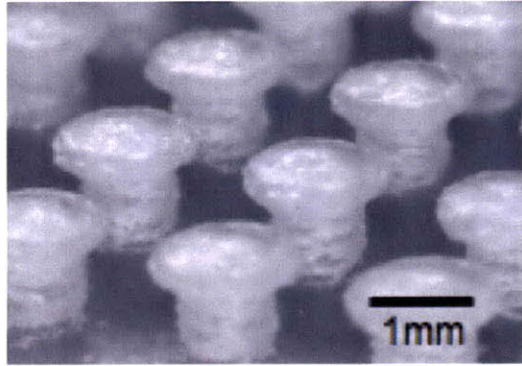


Figure 3.1 Three-dimensionally printed millihoodoos.

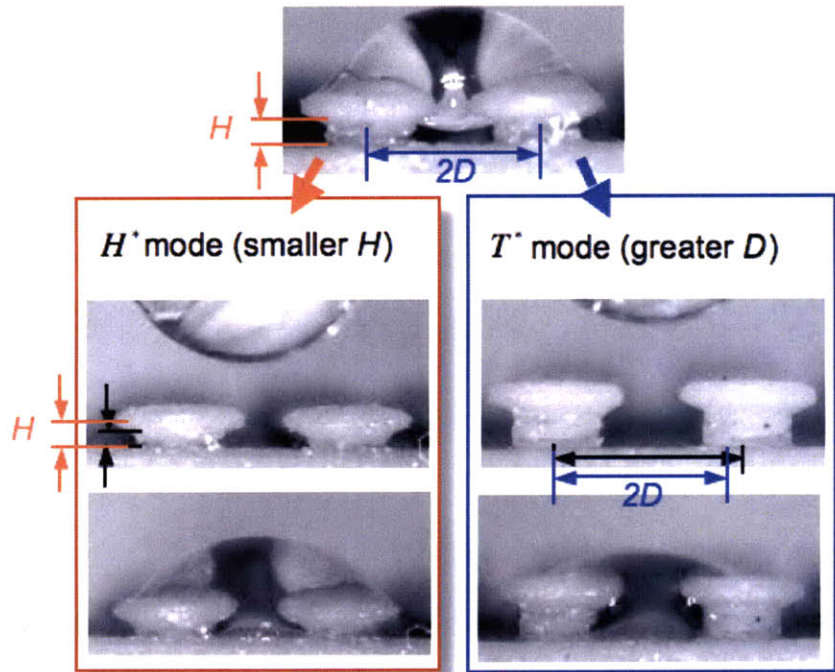


Figure 3.2 The Cassie-Baxter state droplet (top) and sequential images of two failure modes (bottom).

The two failure modes are shown clearly in the Figure 3.2. The top image exhibits the Cassie-Baxter state of an ethanol droplet and the distorted liquid-air interface under the droplet. From the design in the top image, the height or spacing of

millihoodoos was changed first. The images on the left side are representing the sequential results of placing an ethanol droplet on the hoodoos possessing a height shorter than the design in the top image. When the droplet approaches the hoodoo cap parts, the lowest point of the liquid-air interface touches the bottom of solid between the hoodoos just before the other parts of the interface reach the hoodoo cap parts. Once the contact occurs, it leads to a spontaneous wetting on the solid surface. As a result, the Wenzel state of the droplet is shown in the bottom image (H^* failure mode).

The other case is when the height of hoodoos is great enough to prevent the first failure mechanism. The composite contact line first reaches the point of the minimum texture angle (ψ_{\min}) before the lowest part of liquid-air interface wets the bottom solid surface. This case leads to another instantaneous wetting from the point of the minimum texture angle because the curvature of liquid-air interface cannot resist greater pressure difference across the interface (T^* failure mode).

In addition to observation of the transition from the Cassie-Baxter state to Wenzel state, we have employed a three-dimensional printing technique for the fabrication of the structure negative minimum texture angle, as shown in the Figure 3.3. As mentioned in the Chapter 2 Methodology, in the three-dimensional printing process, the supporting material that is deposited to support re-entrant (or overhang) structure is dissolved after the UV-curing step. Thereby, this method can produce a variety of structures including spade and club shape in the below since the UV-curable polymer droplets are deposited without any limit in three dimension thanks to the supporting material. Note that the below two-dimensional images are the cross-sectional views of the three-dimensional structures.

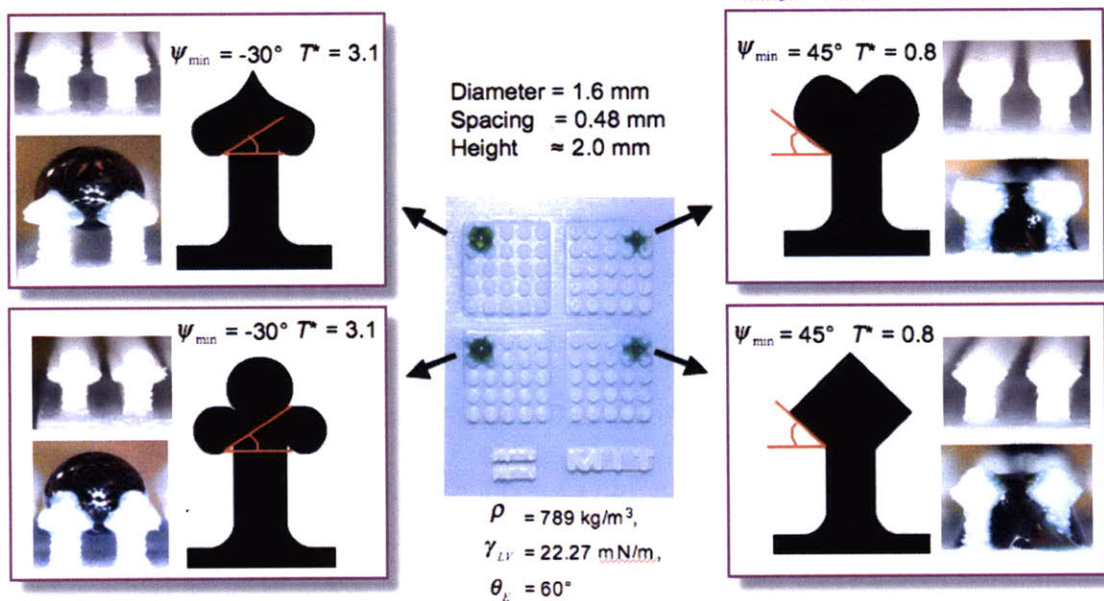


Figure 3.3 Ethanol droplets with green dye on the textured surfaces with four card shapes shows the effect of negative minimum texture angles (ψ_{\min}) on the two wetting regimes.

Four different card shapes were three-dimensionally printed and coated with fluorodecyl-POSS. As shown in Figure X, ethanol droplets (volume $\sim 10 \mu\text{l}$) with green dye were gently placed on top of the square array of each structure. The height of pillar part, diameter of cap part, and the period of square array are kept to be identical in the four shapes. Therefore the different results on the four card shapes represent the effect of the minimum texture angle on the wettability of the textured surfaces. As expected, ethanol droplets form the Cassie-Baxter state on both the spades and clubs whose $\psi_{\min} = -30^\circ$, whereas the droplets were not supported by both the hearts and diamonds whose $\psi_{\min} = 45^\circ$, immediately as the droplets are placed on top of the solid structure.

The overall results are analyzed by using the dimensionless robustness parameters in the Figure 3.4. Note that since the diameter of the hoodoo cap part (W), the radius of curvature of the hoodoo cap part (R) and the volume of droplets are fixed in this experiment. Therefore, the expression for H^* depends on only H and D , which are the two axes of the Figure 3.4. In particular, the T^* failure mode depends only on D because it is assumed that H is large enough to prevent H^* failure in this case.

However, the specific values of H^* and T^* are not consistent with the meaning of values of the dimensionless robustness parameters. We expected that failures occur when H^* and T^* is about 1 where the critical pressure difference of droplets on the surface topography is around the value of the reference pressure difference. But the existing formulae have turned out that they lead to unexpected values of H^* and T^* . Ethanol droplets failed on the millihoodoos even when H^* is equal to 12.3.

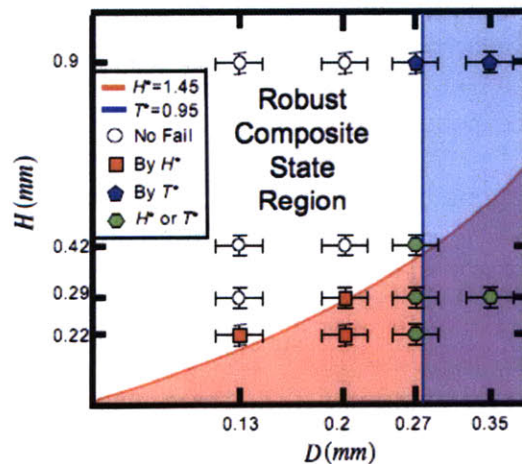


Figure 3.4 The overall results of millihoodoo experiment with theoretical prediction based on the dimensionless robustness parameters derived for microhoodoos.

3.4 Derivation of dimensionless robustness parameters for millihoodoos

Although the dimensionless robustness parameter has been in good agreement with the experiment using microhoodoo surfaces, for analyzing the millihoodoo experiment the results have shown unexpected values. The derivation of the previous formula that were optimized for microhoodoo surfaces was checked and it turned out that some assumptions in the derivation are not appropriate because of the significant differences between microhoodoo and millihoodoo.

First, the shape of the hoodoo cap is different. The previous formula is based on the square top view shape of microhoodoo cap but the millihoodoo caps have round top view shapes. At a first glance this looks a minor or even negligible factor; however, the combination of relatively great diameter of the hoodoo cap ($2W$) and small spacing ($2D$) of round cap shaped hoodoo (millihoodoo case) leads to about five times greater spacing between two diagonally adjacent hoodoos compared to the square cap shaped hoodoo (microhoodoo case). This greater spacing is one of the major reasons that cause a smaller resistance against pressure difference across the liquid-air interface between hoodoos despite of the high values of H^* .

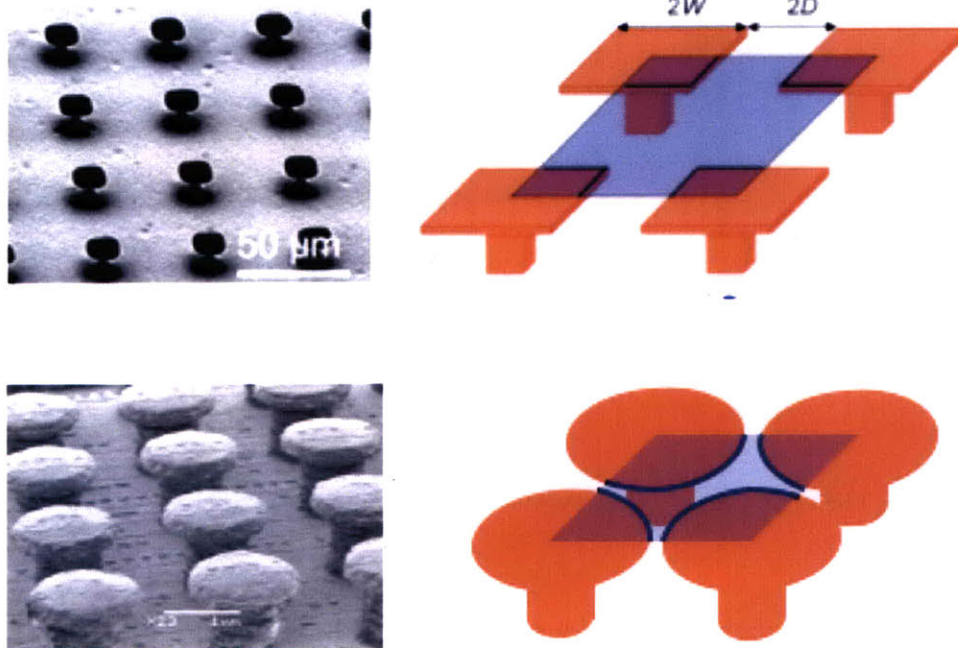


Figure 3.5 The scanning electron microscope (SEM) images and schematic oblique view of microhoodoos and millihoodoos. The upper illustration describes the unit area for the calculations of the dimensionless robustness parameters [28] and the lower illustration shows an important difference compared to the square hoodoos. The diagonal distance between the edge of two hoodoo cap parts is much greater than the horizontal or vertical distance between them (in case of top view).

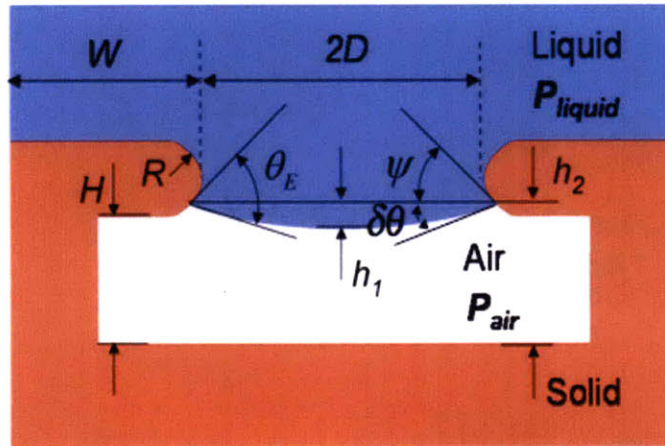


Figure 3.6 The cross-sectional view of hoodoo geometry and some notations [28].

Second, the relative dimensions (R , W , D , and H in Figure 3.6) of the hoodoo structures also attributes the distorted values calculated based on the previous theory on robustness. Whereas the microhoodoos have a negligible thickness ($2R$) of cap parts, millihoodoos possess relatively great thickness, which affects the vertical position of the lowest liquid-air interface. Thus this difference between the calculated vertical position and real position of the lowest liquid-air interface becomes another source that causes unexpectedly high H^* values of millihoodoo surfaces.

Based on the observation and understanding the reasons of misleading values, the generalized dimensionless robustness parameters have been derived from the derivation of H^* and T^* in the paper [28] and then particular values for the millihoodoo structure have been substituted. First, using the notations in Figure 3.6, H^* for a striped hoodoo structure is derived first and then extended to discrete hoodoos with the round top view shape of hoodoo caps.

Although the previous derivation has ignored R (the radius of curvature of the hoodoo cap side), it cannot be negligible because R is on the order of H .

$$P_H \cdot 2\{D + R(1 - \sin \psi)\}L = \gamma_{LV} \cdot 2L \cdot \sin \delta\theta_{\text{stripe}} \quad (3.4-1)$$

Simply, the following equation is obtained from (3.4-1) and correlated with the Laplace Pressure.

$$P_H = \frac{\gamma_{LV} \sin \delta\theta_{\text{stripe}}}{D + R(1 - \sin \psi)} = \frac{\gamma_{LV}}{R_{\text{sag}}} \quad (3.4-2)$$

From the derivation in the paper (Figure S7 [28]), if the simplification using the approximation is changed to the original trigonometric relation the following relation is determined.

$$R_{\text{sag}} = \frac{2 \sin^2(\delta\theta / 2) \cdot [D + R(1 - \sin \psi)]^2}{\sin^2(\delta\theta) \cdot [R(1 - \cos \theta_E) + H]} \quad (3.4-3)$$

By substituting Eq. 3.4-3 into Eq. 3.42, the critical pressure difference for the H^* case is calculated.

$$P_H = \frac{\gamma_{LV}}{R_{\text{sag}}} = \frac{\gamma_{LV} \sin^2(\delta\theta) \cdot [R(1 - \cos \theta_E) + H]}{2 \sin^2(\delta\theta / 2) \cdot [D + R(1 - \sin \psi)]^2} \quad (3.4-4)$$

$$H^* = \frac{P_H}{P_{\text{ref}}} = \frac{\ell_{\text{cap}} \sin^2(\delta\theta) \cdot [R(1 - \cos \theta_E) + H]}{4 \sin^2(\delta\theta / 2) \cdot [D + R(1 - \sin \psi)]^2} \quad (3.4-5)$$

Next step is for the discrete hoodoos with the round top view shape. Eq. 3.4-1 is represented as the following.

$$P_H \cdot \left[\{W + D(1 - \sin \psi)\}^2 - \frac{\pi \{W - R(1 - \sin \psi)\}^2}{4} \right] \quad (3.4-6)$$

$$= \gamma_{LV} \cdot \frac{2\pi[W - R(1 - \sin \psi)]}{4} \cdot \sin \delta\theta_{discrete}$$

For the expression for the incremental sagging angle $\delta\theta_{discrete}$ the two Eqs. 3.4-1 and 3.4-5 are compared and then rearranged.

$$\sin \delta\theta_{stripe} = \frac{2 \sin \delta\theta_{discrete}}{\left[\frac{W - R(1 - \sin \psi)}{D + R(1 - \sin \psi)} \right] \left[\frac{4}{\pi} \left\{ 1 + \left(\frac{D + R(1 - \sin \psi)}{W - R(1 - \sin \psi)} \right) \right\}^2 - 1 \right]} \quad (3.4-7)$$

Lastly, by substituting the Eq. 3.4-6 into Eq. 3.4-2, we have calculated P_H for the discrete hoodoo case and then compared with the reference pressure of an ethanol droplet to derive the final form of H^* .

$$H^* = \frac{\left[\frac{\sin^2(\delta\theta)}{2 \sin^2(\delta\theta / 2)} \right] R \ell_{cap} \left[(1 - \cos \theta_E) + \frac{H}{R} \right]}{[D + R(1 - \sin \psi)]^2 \left[\frac{W - R(1 - \sin \psi)}{D + R(1 - \sin \psi)} \right] \left[\frac{4}{\pi} \left\{ 1 + \left(\frac{D + R(1 - \sin \psi)}{W - R(1 - \sin \psi)} \right) \right\}^2 - 1 \right]} \quad (3.4-8)$$

The last part is the derivation of T^* using the similar steps based on the Eq. s4-10 in the literature. Note that R is not ignored here again because of the same reason in the derivation of Eq. 3.4-1.

$$P_\theta \cdot 2\{D + R(1 - \sin \psi)\}L = \gamma_{LV} \cdot 2L \cdot \sin(\theta_E - \psi_{min}) \quad (3.4-8)$$

Similar to Eq. 3.4-2, the terms in Eq. 3.4-8 are rearranged.

$$P_\theta = \frac{\gamma_{LV} \sin(\theta_E - \psi_{min})}{D + R(1 - \sin \psi)} \quad (3.4-9)$$

Compared with the reference pressure, T^* for the striped hoodoo with considerable R is calculated.

$$T^* = \frac{P_\theta}{P_{ref}} = \frac{\ell_{cap} \sin(\theta_E - \psi_{min})}{2[D + R(1 - \sin \psi)]} \quad (3.4-10)$$

Finally, we have extended the discussion of T^* for the discrete hoodoo possessing round cap shape (top view) by substituting the Eq. 3.4-7 and employing the similar method used in Eq. 3.4-8.

$$T^* = \frac{\ell_{cap} \sin(\theta_E - \psi_{min})}{[D + R(1 - \sin \psi)] \left[\frac{W - R(1 - \sin \psi)}{D + R(1 - \sin \psi)} \right] \left[\frac{4}{\pi} \left\{ 1 + \left(\frac{D + R(1 - \sin \psi)}{W - R(1 - \sin \psi)} \right) \right\}^2 - 1 \right]} \quad (3.4-11)$$

The following formulae are the simplified H^* and T^* by substituting the conditions for millihoodoos.

$$H^* = \frac{3\ell_{cap}H}{2DW \left[\frac{4}{\pi} \left(1 + \frac{D}{W} \right)^2 - 1 \right]}, \quad T^* = \frac{\ell_{cap} \sin(\theta_E - \psi_{min})}{W \left[\frac{4}{\pi} \left(1 + \frac{D}{W} \right)^2 - 1 \right]} \quad (3.4-12)$$

3.5 Quantitative analysis

The Figure 3.7 is the overall result using the rederived H^* and T^* . Note that in our experiment, W is fixed, therefore H^* depends on H and D whereas T^* is affected by D only. First of all, horizontal axis indicates spacing D of millihoodoo and vertical axis indicates height H . On this red line, all the points have identical H^* value of 1.25 which is the average value of this range and in this light red area, H^* value is smaller than 1.25. This means H^* failure would occur. Next on this blue line, all the points have identical T^* value of 1 which is the average value of this range and in this light blue

area T^* failure would occur due to the larger spacing. Therefore, only white region possessing large H and small D represents Cassie-Baxter state.

As shown in the Figure 3.7, these specific values are near 1 and in good agreement with experimental results, no failure, H^* failure, T^* failure and failure by H^* or T^* . Actually, these specific values are also verified by using simulation models in the next section.

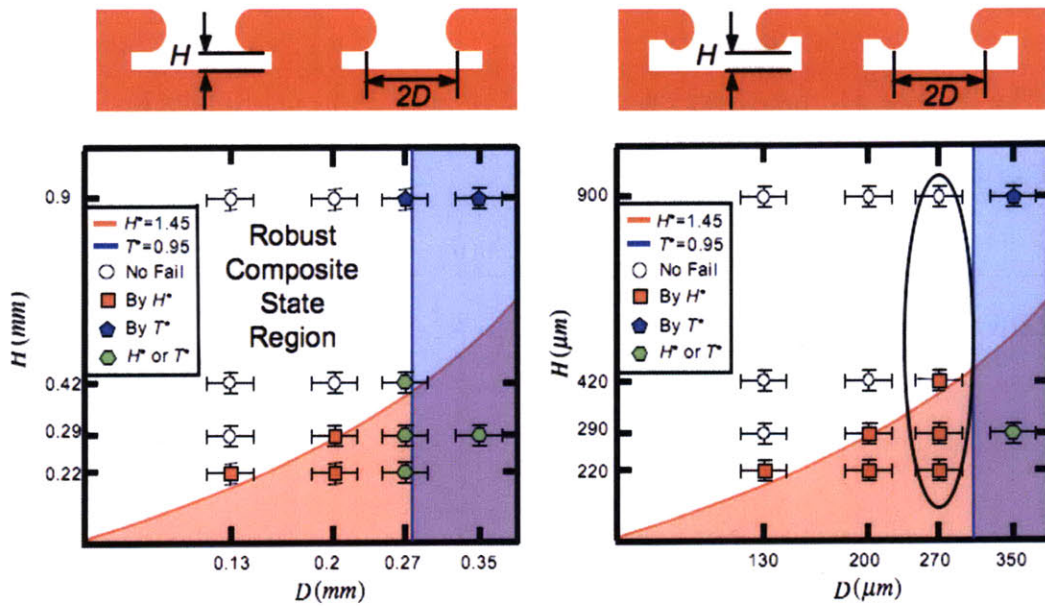


Figure 3.7 The overall results of millihoodoo experiment with theoretical prediction based on the generalized dimensionless robustness parameters. (a) standard hoodoo geometry. (b) re-entrant geometry with negative texture angle ($\psi = -90^\circ$) possessing the identical values of height (H) and spacing ($2D$).

Chapter 4

4. Simulation of Static Wetting Phenomena

In this chapter, the input routines (or source codes) for modeling a liquid droplet on hoodoos at multiple length scales are explained in detail. Developed by using finite element method based simulation software the Surface Evolver, the millihoodoo and nanohoodoo models compute the equilibrium state shape of liquid droplets. In addition, they provide the verification of two failure modes at different length scales and *a priori* evaluation of robustness of the Cassie-Baxter composite state of droplets on re-entrant structures.

4.1 Hoodoo structure

Input routines that describe a droplet sitting on four identical hoodoo structures were coded by using the Surface Evolver grammar in text (.txt) file format. For the development of the simulation model, mathematical symmetry around an axis was used because the droplet is placed at the center of a square array of four hoodoos. Using the mirror and transform commands, the liquid drop and re-entrant structure are represented by only one eighth of the entire geometry, thereby saving computation resources (Figure 4.1).

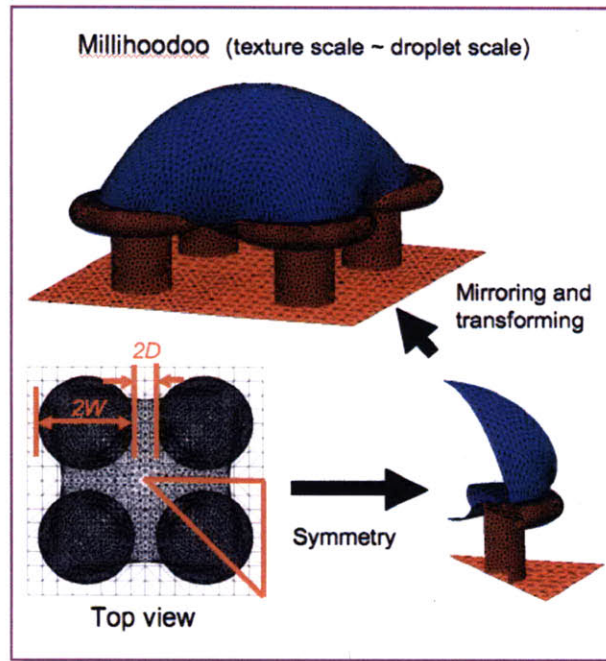


Figure 4.1 The liquid-air-solid composite system including four millihoodoos.

```
constraint xmirror_con
formula: x=0
```

```
constraint ymirror_con
formula: y=2*(Ww+Dd)
```

```
view_transform_generators 1
1 0 0 0 // 1/8 clockwise
0 1 0 0
0 0 1 0
0 0 0 1
```

```
view_transform 1
1 0 0 0 // 1/8 clockwise
0 1 0 0
0 0 1 0
0 0 0 1
```

(The full source code of transform command is omitted here. See Appendix.)

The geometry including the part of a hoodoo and a droplet defined in the Surface Evolver is composed of three parts. First, the bottom of the solid is produced by only three points (or vertices referred as points in the Surface Evolver command system) and then connected by lines (or edges). To capture T^* failure mode using the bottom view, no opaque color was used for the bottom facet. In other cases, the bottom facet (or face) is filled with red color to clearly show the bottom solid for making some movies and helping understand the structure of the liquid-air-solid composite system.

vertices

```

2 0          0          0 constraints diagmirror_con xmirror_con
3 2*(Ww+Dd) 2*(Ww+Dd) 0 constraints diagmirror_con ymirror_con
4 0          2*(Ww+Dd) 0 constraints ymirror_con xmirror_con

```

edges

```

520 2 3 constraints diagmirror_con
530 3 4 constraints ymirror_con
540 4 2 constraints xmirror_con

```



Figure 4.2 Bottom facets for the millihoodoo model (red).

Second, the pillar of hoodoo structure is created using a simple formula describing a cylinder. The constraints including surface tension were imposed only on the sidewall that is colored by red. The height (H) of the hoodoo structure is adjusted in each simulation indirectly by using several “bottom surfaces,” which help to measure the critical height of the hoodoo structure in the case of failure.

```

parameter Hh          = 0.800 *0.001 // millimeter
parameter Hh_top      = 0.928 *0.001 // millimeter
parameter Hh_bottom   = 0.672 *0.001 // millimeter
parameter Hh2         = (0.672-0.1) *0.001 // millimeter
parameter Hh3         = (0.672-0.2) *0.001 // millimeter
parameter Hh4         = (0.672-0.3) *0.001 // millimeter

```

```

constraint pillar_con
formula: (x-Ww-Dd)^2+(y-Ww-Dd)^2=((Ww-Rr)/2)^2

```

(The source code of vertices and other components are omitted here. See Appendix.)



Figure 4.3 Pillar facets for the millihoodoo model (red).

Third, the cap of hoodoo structure is composed of three surfaces: top flat surface, side donut surface, and bottom flat surface. The surfaces that are contacted with a liquid droplet is identified as wetted area and colored as blue, whereas the other area is assumed to be dry and colored by red. All the surfaces are designed as smooth surfaces and the edges of each surface are connected by specific constraints; therefore the liquid-air-solid contact line can move along the surfaces in order for the composite system to be in an equilibrium position as other constraints like the volume of a liquid droplet are set. Finally, the droplet was placed at the center of the square array of four hoodoos as a polyhedron and given blue color.

constraint torus_con //clockwise(1/4)
 formula: $((x)^2+(y)^2)^{0.5}-(Ww-Rr)^2+(z-Hh)^2=Rr^2$

constraint top_con
 formula: $z=Hh+Tt$

constraint bottom_con
 formula: $z=Hh-Tt$

faces
 1 1 2 3 constraints top_con tension
 $tens*0.5*(1-\cos(\text{angle}*\pi/180))$ color blue

11 11 12 13 -2 constraints top_con
 tension $tens*0.5*(1-\cos(\text{angle}*\pi/180))$ color blue

21 21 22 23 -12 constraints torus_con
 tension $tens*0.5*(1-\cos(\text{angle}*\pi/180))$ color blue

31 31 32 33 -22 constraints torus_con
 tension $tens*0.5*(1-\cos(\text{angle}*\pi/180))$ color blue

41 501 502 503 -32 constraints tension tens color blue

101 -103 -102 -101 constraints bottom_con
 tension $tens*0.5*(1+\cos(\text{angle}*\pi/180))$ color red

```
111 102 -113 -112 -111 constraints bottom_con
tension tens*0.5*(1+cos(angle*pi/180)) color red
```

```
121 112 -123 -122 -121 constraints torus_con
tension tens*0.5*(1+cos(angle*pi/180)) color red
```

```
131 122 -133 -32 -131 constraints torus_con
tension tens*0.5*(1+cos(angle*pi/180)) color red
```

(The source code of vertices and other components are omitted here. See Appendix.)

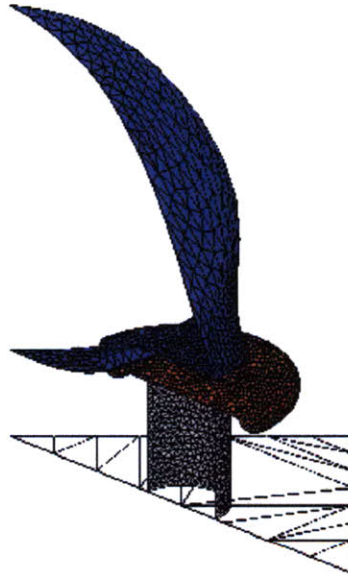


Figure 4.4 Top facets for the millihoodoo model (blue and red).

The polyhedron structure of the droplet evolves into a distorted sphere shape that is constrained by the gravity acting on the mass of the droplet or pressure difference across the liquid-air interface, at each iteration. When the sixth decimal place in the value of energy (second column in Figure 4.5) reached constant number, the iteration process was stopped because the change of the droplet shape by more iteration

is negligible. The equilibrium contact angle is preserved locally and determined by the constraints of surface tension at each interface: liquid-air, liquid-solid, and solid-air interface. To simulate the quasi-static and isothermal evaporation of an ethanol droplet, we investigated the behavior of a series of droplets, by decreasing the volume of the droplet until they reached one of the failure modes.

bodies

```
1 -1 -11 -21 -31 -41 pressure 0.2*press
```

```
gogo := {
```

```
body[1].pressure := press; g 30; hessian_seek; hessian_seek; V; V; }
```

```
Terminal — evolver — 80x24
1. area: 6.13493360065025e-07 energy: 2.21972168965418e-07 scale: 0.00156369
Vertex averaging done.
Vertex averaging done.
30. area: 6.13496563887374e-07 energy: 2.21972189074232e-07 scale: 14.9645
29. area: 6.13496452099295e-07 energy: 2.21972188430423e-07 scale: 11.8536
28. area: 6.13496357432902e-07 energy: 2.21972187787877e-07 scale: 14.8807
27. area: 6.13496251996702e-07 energy: 2.21972187145583e-07 scale: 11.8622
26. area: 6.13496153808602e-07 energy: 2.21972186503455e-07 scale: 14.8492
25. area: 6.13496050641040e-07 energy: 2.21972185861329e-07 scale: 11.8784
24. area: 6.13495952323437e-07 energy: 2.21972185219181e-07 scale: 14.8224
23. area: 6.13495850156312e-07 energy: 2.21972184576920e-07 scale: 11.8955
22. area: 6.13495752183399e-07 energy: 2.21972183934532e-07 scale: 14.7968
21. area: 6.13495650593587e-07 energy: 2.21972183291940e-07 scale: 11.9126
20. area: 6.13495553048459e-07 energy: 2.21972182649131e-07 scale: 14.7719
19. area: 6.13495451771173e-07 energy: 2.21972182006033e-07 scale: 11.9296
18. area: 6.13495354606497e-07 energy: 2.21972181362635e-07 scale: 14.7475
17. area: 6.13495253472918e-07 energy: 2.21972180718867e-07 scale: 11.9465
16. area: 6.13495156599773e-07 energy: 2.21972180074717e-07 scale: 14.7234
15. area: 6.13495055406383e-07 energy: 2.21972179430119e-07 scale: 11.9631
14. area: 6.13494958807268e-07 energy: 2.21972178785061e-07 scale: 14.6999
13. area: 6.13494857616477e-07 energy: 2.21972178139477e-07 scale: 11.9796
12. area: 6.13494761038490e-07 energy: 2.21972177493358e-07 scale: 14.6767
```

Figure 4.5 Snapshot of the terminal window for Surface Evolver (Mac OS™ version).

The iteration routine using the Surface Evolver offers some advantages and disadvantages. First of all, the sectioned geometry shows the cross-sectional view of the resulting shape of droplets as well as saves computational resource. Moreover, the

averaged size of each facet is also controllable, leading to more accurate calculation.

On the contrary, there are some limitations in describing advancing and receding contact angles because the motion of contact line is not considered in this routine. Therefore, to simulate dynamic wetting phenomena, further advanced modeling should be applied into this routine in the future work. The entire source of code is attached in the appendix.

4.2 Comparison with experimental results

The simulation results were compared with the experimental results of Chapter 3, assuming the identical physicochemical properties of the droplets-air-millihoodooos composite system and substituting the gravitational acceleration of 9.8m/s^2 .

Each point in the Figure 3.7 is verified and categorized into two failure modes by observing the equilibrium shape of the liquid droplets in the simulation. The cross-sectional side view to display the lowest point of liquid-air interface and the bottom view to observe the liquid-air-solid composite contact lines are checked after a sufficient number of iteration. The results are generally in good agreement with the millihoodoo experiment. Some discrepancy may be from the different surface roughness; because of the low accuracy of three-dimensional printing technology used in the experiment, the micrometric roughness produces continuous small re-entrant structure on the side of millihoodooos and therefore influences the robustness of the composite state of droplets.

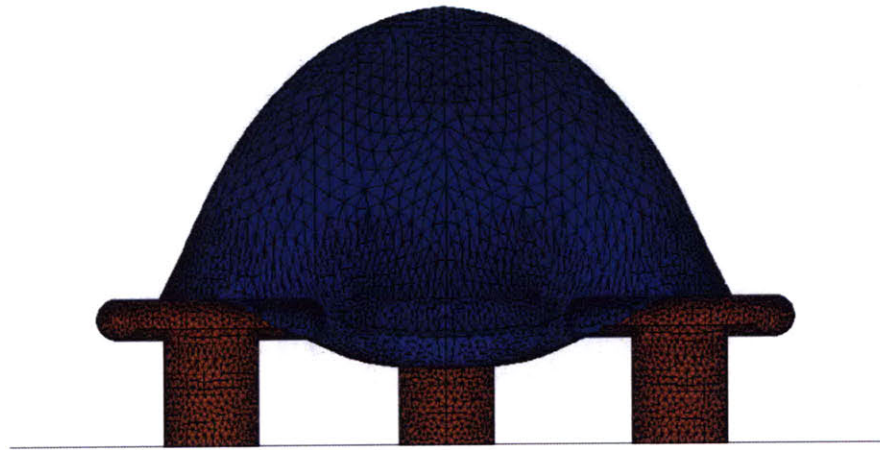


Figure 4.6 The cross-sectional view of a droplet and millihoodoos (a snapshot in the middle of the calculation for an equilibrium state).

4.3 Application of the simulation model at the nanometric scale

The core part of the iteration routine can also be applied to the prediction of the two failure modes or *a priori* evaluation of the robustness of the Cassie-Baxter composite state at the nanometric scale. As shown in the Figure 4.7, four nanohoodoos which are arranged in a square array support a part of liquid-air interface of a droplet. Note that there are more than billions of nanohoodoos under a millimetric liquid droplet because the texture scale is much smaller than the droplet scale.

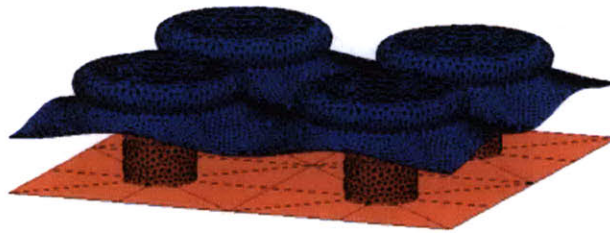


Figure 4.7 The oblique view of liquid-air-solid composite system including four nanohoodoos and a part of liquid-air interface.

The main difference in the source code for nanohoodoo (compared to that for millihoodoo) is the way to impose pressure difference across the liquid-air interface. Whereas the volume of the droplet and the density of liquid lead to the pressure difference by gravitational field, substituting the value of pressure of liquid against air results in the distorted liquid-air interface. This method is clearly more cost-efficient than describing an enormous liquid droplet with billions of nanohoodoos. The other physico-chemical properties of composite system are kept as the millihoodoo model and thus the following two major results are considered to predict wetting phenomena at the nanometric scale.

The two failure modes are verified at the nanometric scale, which was predicted by the robustness analysis in the literature. First, this nanohoodoo model clearly showed two different modes which is schematically shown in the Figure 4.8. Moreover, the critical pressure and kinds of failure calculated by using the nanohoodoo model were consistent with the order of magnitude of breakthrough pressure obtained from the

microhoodoo experiment when the scale of design parameters is adjusted to become the value used in the PNAS paper.



Figure 4.8 Schematic overview of two failure mechanisms and criteria - the texture angle (ψ) and height of the lowest point of liquid (h).

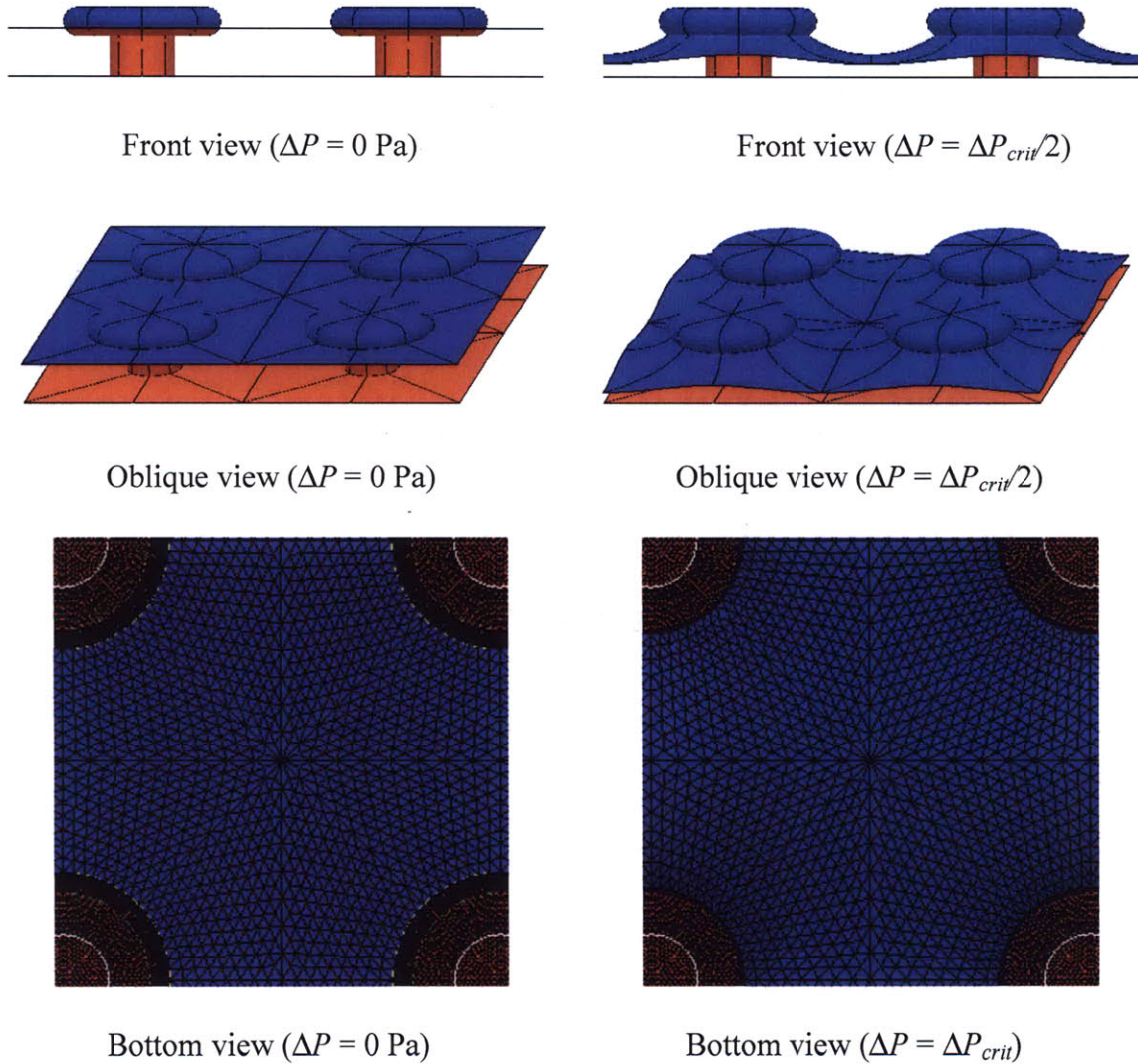


Figure 4.9 Movie frames showing two kinds of failure mechanisms (nanohoodoo case).

The consistency of these hoodoo models with milli/microhoodoo experiments supports our final goal in this section: the development of reliable *a priori* evaluation of robustness of the composite state droplet on nanohoodoos. As shown in the Figure 4.10, the proposed nanohoodoo design can support an ethanol droplet up to the breakthrough pressure of about 26 kPa. It should be noted that the texture angle (ψ) at the liquid-air-solid contact line reaches zero degrees, which is equal to the minimum value of the

hoodoo structure and means T^* failure, before the lowest part of liquid-air interface contacts the bottom solid ($h = 0$).

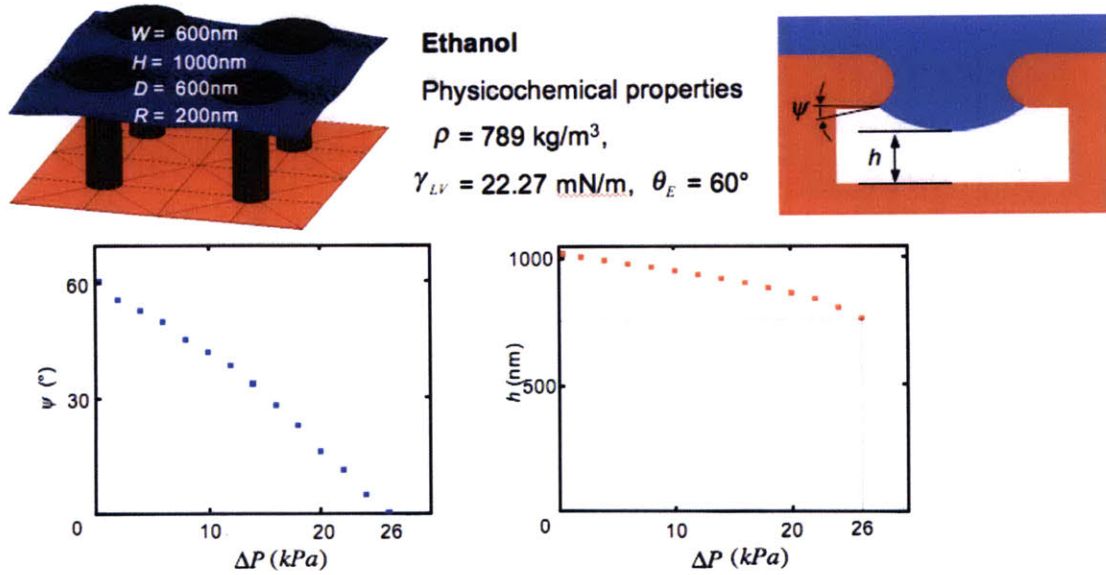


Figure 4.10 Calculation of the texture angle (ψ) and height of the lowest point of liquid (h) with respect to pressure difference across the liquid-air interface of a millimetric droplet on nanohoodoos.

At last, it is important to emphasize the meaning of the breakthrough pressure of 26 kPa. This value is more than five hundred fold compared with the breakthrough pressure of microhoodoo surfaces. Considering the fact that the pressure under 10 cm of water is about 1 kPa, the microhoodoo surface ($P_{breakthrough} = \Delta P_{crit} \sim 100 \text{ Pa}$) is not practical for our daily life. However, the result of simulation model opens a pathway to significantly improve the robustness of composite state on non-wettable surfaces and expand application of liquid repelling solid surfaces under harsh circumstance including rain drop impact.

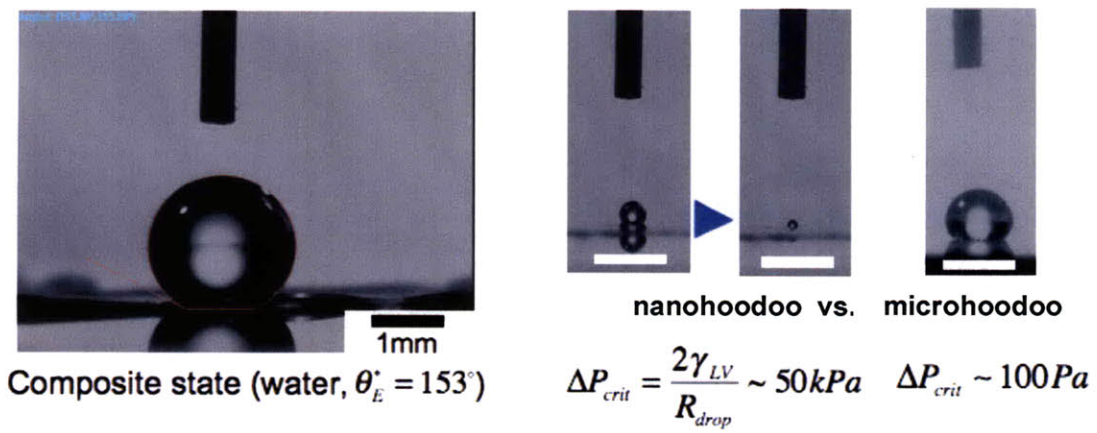


Figure 4.11 Increase in the robustness of Cassie-Baxter composite state on a nanohoodoo surface compared to a microhoodoo surface. The white scale bars in the three small images indicate 1mm.

Chapter 5

5. Dynamic Robustness

To investigate the robustness of the Cassie-Baxter state liquid droplets that impact on textured surfaces, water droplets were dropped on transparent superhydrophobic nanopost surfaces by the gravity. In addition to the observation of side and bottom view of the drop impact utilizing a beam splitter, the impact forces were measured using a piezoelectric film pressure sensor at the impact velocity ranging from 0.99 m/s to 1.47 m/s. Based on the experimental results, the modified coefficient of the water hammer pressure is proposed.

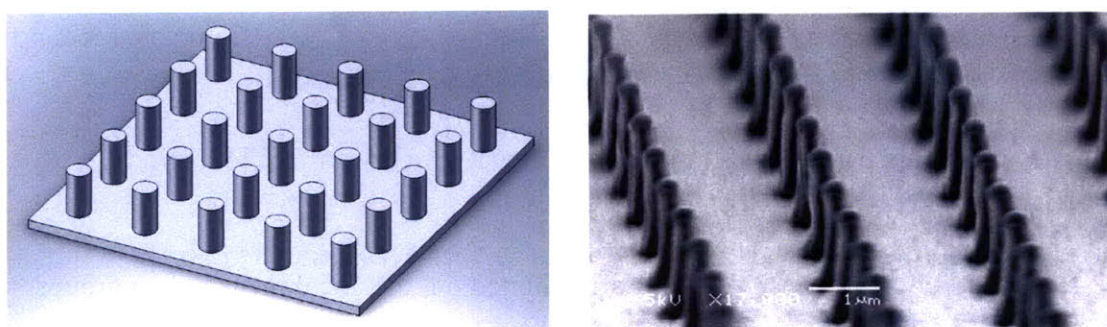


Figure 5.1 Schematic drawing image of a square array of posts and SEM image of nanoposts made of PFPE.

Before discussing the method to calculate the maximum impact pressure and its experimental verification, some of important arguments should be noted. According to

the experiments of Rioboo *et al.*, there are six possible outcomes of drop impact as shown in Figure 5.2. In this work, the last two rows – partial rebound and complete rebound – are focused for the verification of our theoretical approach.

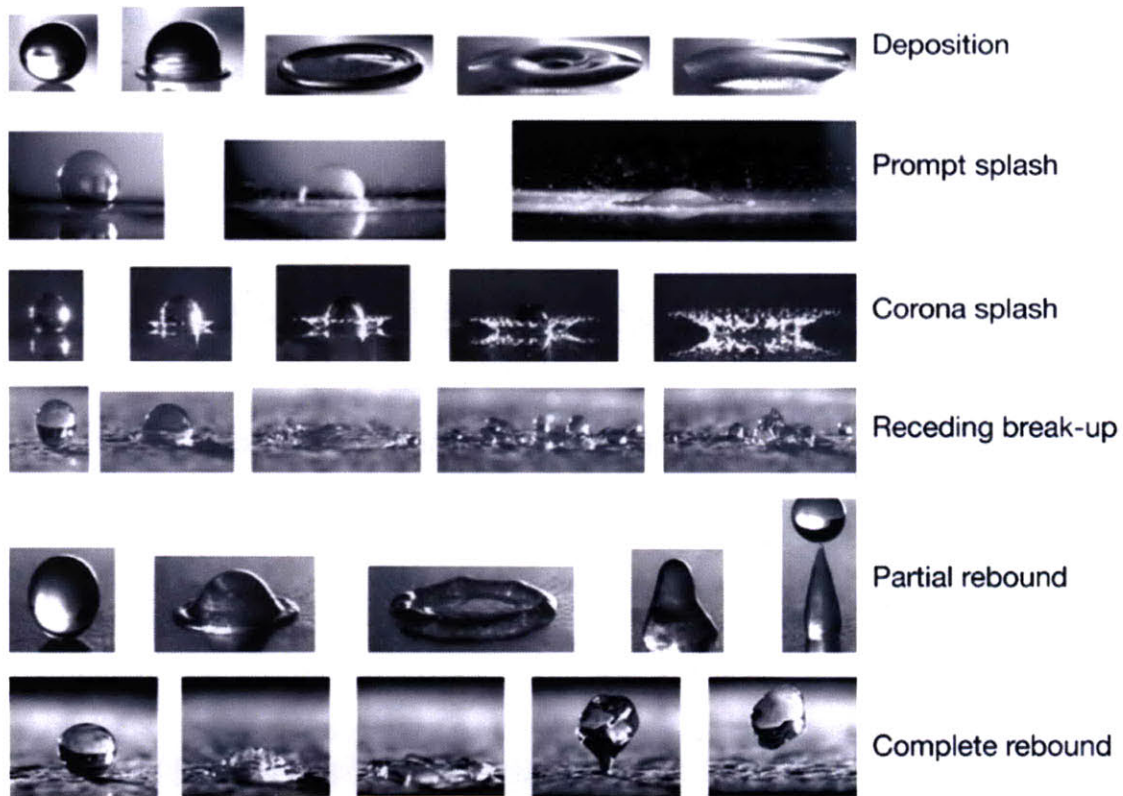


Figure 5.2 Morphology of drop impact on a dry surface [51, 69].

In addition, Rioboo *et al.* and Yarin pointed out that the dimensionless groups Weber number (We), Reynolds number (Re), and Ohnesorge number (Oh) can not accurately describe the six different outcomes in Figure 5.2, although the non-dimensionalized numbers play an essential role for the analysis of motion of droplets on flat surfaces. This is because the dimensionless groups do not have information about the

wettability and roughness of solid surface, which is closely related to the behavior of droplets.

$$We = \frac{\rho DV_0^2}{\sigma} = \frac{\text{inertial effect}}{\text{surface tension effect}} \quad (5-1)$$

$$Re = \frac{\rho DV_0}{\mu} = \frac{\text{inertial effect}}{\text{viscous effect}} \quad (5-2)$$

$$Oh = \frac{\mu}{(\rho\sigma D)^{1/2}} = \frac{We^{1/2}}{Re} \quad (5-3)$$

where V_0 and D denote the drop diameter and impact velocity, respectively, ρ , σ and μ liquid density, surface tension and viscosity, respectively.

Instead of the non-dimensional groups, they provided the following Table 5.1, containing the trends of six different outcome indicated by variation of physical parameters. To the extent that this chapter is about dynamic robustness, we will focus on the impact pressure issue rather than the motion of droplets described by the dimensionless groups.

Table 5.1 Summary of the effect of each parameter on each of the six scenarios [51, 69]. R_a , R_w and θ_{rec} indicate the roughness amplitude, wave length, and wettability characteristic (receding angle), respectively.

Increase of	Deposition	Prompt splash	Corona splash	Receding breakup	Partial rebound	Complete rebound
V_0	↓	↑	↑	↑	↑	
D	↓	↑				
σ		↓	↓	↑	↑	↑
μ	↑	↓	↓	↓		
R_a	↓	↑	↓			
R_w		↓				
θ_{rec}				↑	↑	↑

5.1 Failure modes and dynamic surface tension

For the consideration of transition from the Cassie-Baxter state to the Wenzel state of a droplet that contacts on the static solid surface with an impact velocity, we assume dynamic failure mechanism is not far different from the static failure mechanism in terms of force balance or maximum pressure difference. The breakthrough pressure should be calculated from the force balance between the surface tension (considering advancing contact angle instead of equilibrium contact angle) and pressure difference across the liquid-air interface, leading to a distorted interface. According to the literature, the dynamic surface tension does not deviate from the 10% of 72 mN/m (Figure 5.3). Thus, the pressure generated by the drop impact can be evaluated to investigate the conditions for the transition using a constant surface tension.

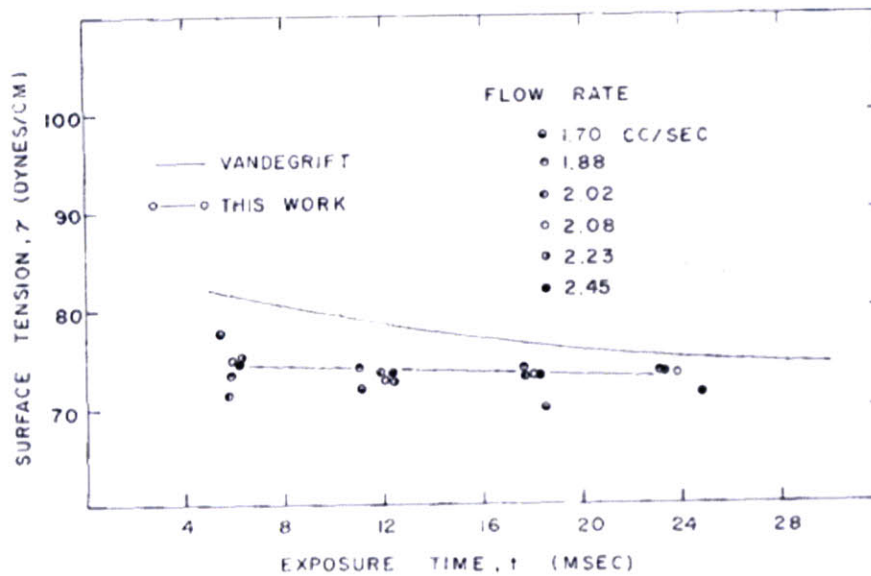


Figure 5.3 Dynamic surface tension of water [70].

5.2 Breakthrough pressure formula for a square array of posts

In their work on water drop impact on superhydrophobic surfaces, Deng *et al.* developed the breakthrough pressure formula using their own notation [57]. They applied this static breakthrough pressure concept to the dynamic situation and attained consistent experimental results. Lee *et al.* also exploited the equation for calculating breakthrough pressure to mention the robustness issue in the analysis of drag reduction [64].

These two representative breakthrough pressure formulae were consistent with the breakthrough pressure formula derived from the dimensionless robustness design parameters except that H^* failure did not appear in those formulae. This is because the researchers assumed that their post structure has high aspect ratio (i.e., the ratio between the height and width of the post) and just considered T^* failure mode (Figure 5.4) [57, 64]. Here are the equations for the critical height of posts to avoid H^* failure and for the breakthrough pressure when T^* failure occurs.

$$H_{crit} = \frac{D(1 - \sin \theta_{adv})}{-\cos \theta_{adv}} \approx 0.27D \quad (5.2-1)$$

$$\Delta P_{breakthrough} = \frac{2\gamma_{LV}(-\cos \theta_{adv})}{D(1 + \sqrt{D^*})} \quad (5.2-2)$$

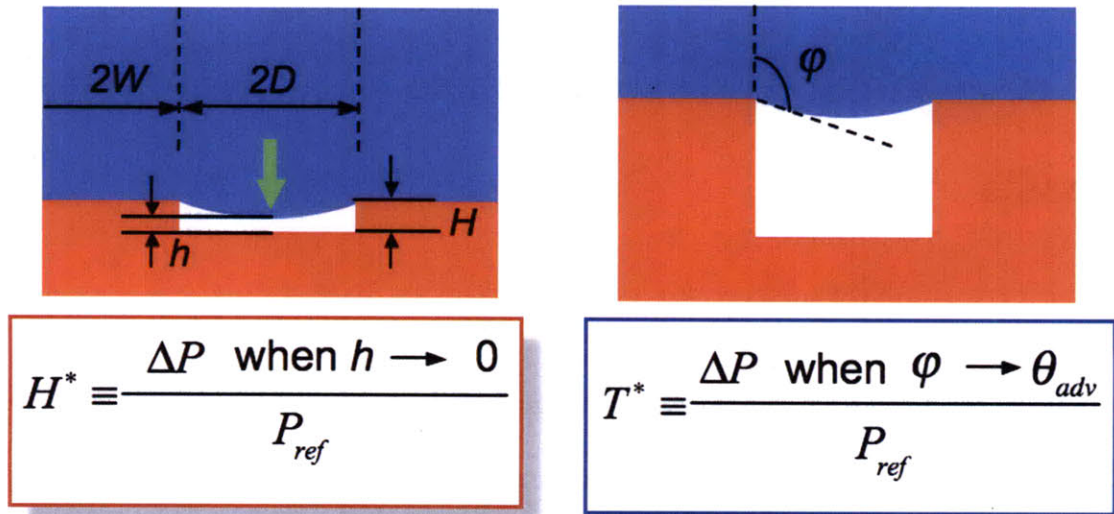


Figure 5.4 Two failure modes of the Cassie-Baxter state droplet on post structure.

5.3 Water hammer pressure

The calculation of water hammer pressure is a more accurate method to compute the maximum dynamic pressure when a water droplet impacts on a solid surface, than the calculation of the Bernoulli pressure. In some recent papers, researchers have used the Bernoulli pressure for calculating the critical impact pressure or velocity for complete rebound but the water hammer pressure has been verified by many experimental studies [46, 55, 56, 65, 71]. Deng *et al.* exploited the water hammer pressure to find the transition condition by comparing it with the intrinsic breakthrough pressure of textured surfaces [57]. They showed that a water droplet completely rebounds off the solid surface after the collision if the water hammer pressure determined by physico-chemical property of the descending water droplet is less than the breakthrough pressure. However, when the drop impact experiment results in the literature ($V_{\text{impact}} \sim 1$ m/s) were compared with the breakthrough pressure of a textured surface based on the static case, the order of magnitude of the water hammer pressure is much higher than the breakthrough pressure, although the water droplets completely rebound. Table 5.2 presents the impact velocity and water hammer pressure calculated assuming the coefficient $\alpha = 0.2$, which was proposed by Engel [53, 54].

Table 5.2 Impact velocities and water hammer pressures.

height (cm)	impact velocity (m/s)	Water hammer pressure (kPa)
1	0.44	132.82
3	0.77	230.04
5	0.99	296.98
7	1.17	351.40
9	1.33	398.45
11	1.47	440.50
13	1.60	478.87
15	1.71	514.39
17	1.83	547.61

In the literature, many complete rebound cases were reported using the superhydrophobic textured surfaces possessing post structure [57, 65]. The researchers calculated that breakthrough pressure was on the order of 1000 Pa and verified this value experimentally, for example, the evaporation of liquid droplet. However, those superhydrophobic textured surfaces could resist the pressure (~ 100 kPa, according to the Table 5.2) by the water droplet that was dropped at the height of several centimeters despite of the breakthrough pressure of several kPa.

We have thought that these discrepancy stems from they adopted the value of water hammer pressure coefficient α from the previous research papers without experimental verification. In the following section, we compared the static breakthrough pressure formulae that were derived in some papers. Then the calculation of impact pressure from the impact force measured on the flat surface utilizing the high-speed camera images.

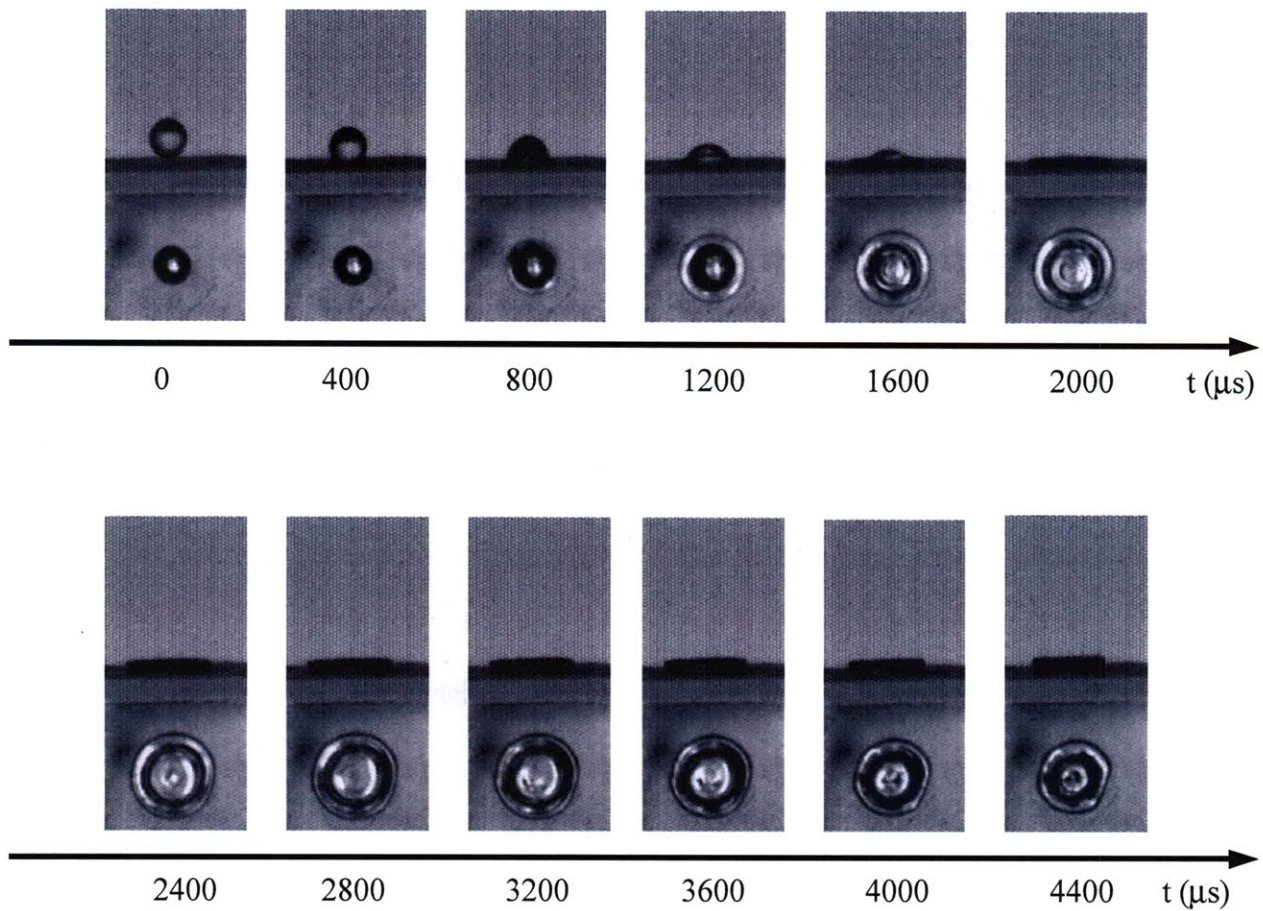
5.4 Drop impact experiment

To verify that the breakthrough pressure formula is also effective in the dynamic contact between water droplets and textured surfaces, the following experiment was designed based on the description in the literature [55, 56]. The impact force was measured using a data acquisition (DAQ) system that was composed of a piezoelectric film (DT2-052K, LEADER Electronics Co.), a DAQ device, and a computer (LabVIEW). This experiment is based on the recent research paper on the measurement of the impact force on hydrophilic flat smooth surfaces [71].

Before water was dropped, the piezoelectric film was calibrated using the simple dynamics equation describing the collision of a rigid ball on a rigid flat surface. In this experiment, the piezoelectric film was attached on the beam splitter that was used for the observation of both side and bottom view. A data acquisition (DAQ) device (National Instruments, USB-6021) collected the voltage information from the piezoelectric film and the LabVIEW 2009 in the computer that was connected to the DAQ device processed the signal. A small stainless steel ball ($m = 1.022$ g, $r = 3.01$ mm) was dropped onto the piezoelectric film at different height to measure the responding voltage (V_o) induced by a wide range of impact force (F_{imp}). Since we used the same piezoelectric film as the film used in the paper, the resultant calibration equation was similar.

$$F_{imp} = 8.58V_o \quad (5.4-1)$$

A nearly constant volume ($V = 8.58 \text{ mL}$) of water ($\rho = 998 \text{ kg/m}^3$, $c = 1500 \text{ m/s}$, $m_{\text{waterdrop}} = 8.58 \times 10^{-6} \text{ kg}$) was released from the syringe tip that was placed above the transparent superhydrophobic nanopost surfaces at different heights with no initial velocity. First, the beam splitter was used to see the bottom view as well as the side view (Figure 5.5). Along with the verification of the circular shape and the complete rebound (i.e., the Cassie-Baxter state) of the spreading water droplet on the superhydrophobic surfaces, both the piezoelectric film and high-speed camera were used to record the voltage signal as well as the motion of the water droplet in the side view.



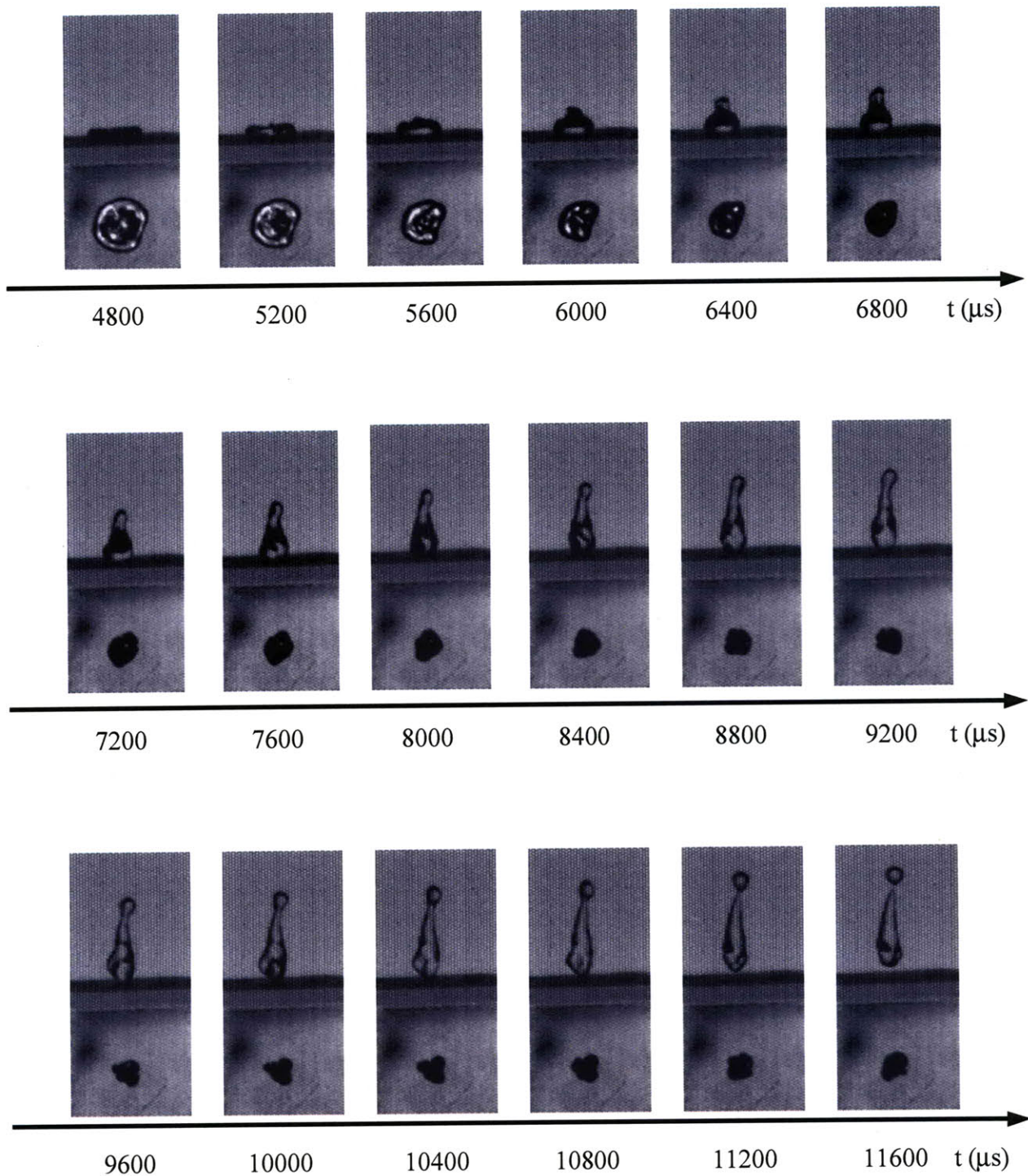


Figure 5.5 Sequential high-speed camera images of the drop impact on superhydrophobic surfaces with the impact velocity of 1.17m/s and the We of 19.0.

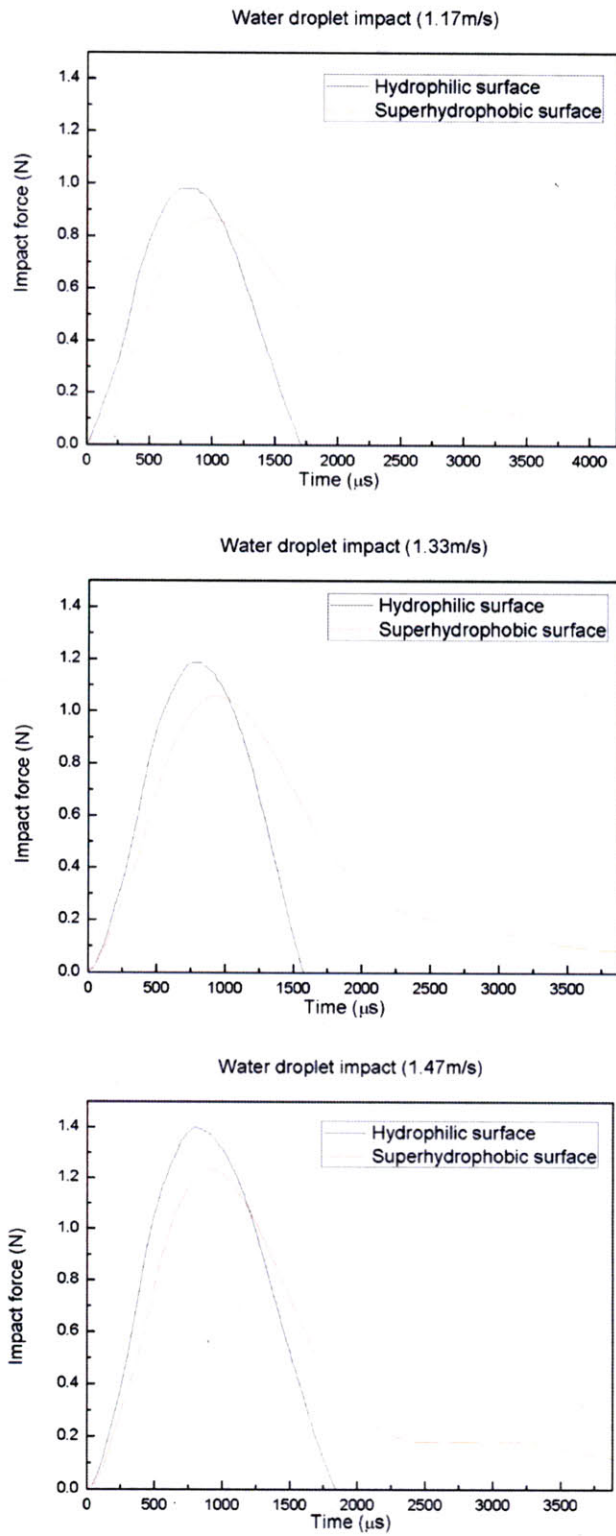


Figure 5.6 Impact force vs. time at various impact velocities.

As shown in Figure 5.6, the temporal distribution of the impact force on the superhydrophobic surface is different from that of the impact force on the hydrophilic surface. The peak impact force on the hydrophilic surface is slightly (10 to 20 percent) higher and faster than the other case. On the hydrophilic surface, the horizontal edge velocity of the water droplet is slow because the drag force acting on the water droplet is stronger than on the textured superhydrophobic surface that possesses a large portion of liquid-air interface as well as the liquid-solid interface. Therefore, most of the momentum is converted into the force in the vertical direction within a shorter time than the superhydrophobic case and it is detected as the impact force by the piezoelectric film. The shorter time duration of the impact force of the hydrophilic surface case can be explained in the similar way.

Although the values of peak impact force are not much different in the two different surface cases, the peak impact pressure might not be similar to each other because the pressure is computed considering the actual area that the force acts on. In other words, the peak point in the temporal distribution of impact pressure does not have to be coincident with that of impact force. However, more deliberate analysis based on the high-speed camera images and other novel method to detect the spatial distribution of impact pressure is necessary because the impact pressure simply calculated from the apparent area does not represent the local maximum pressure that is highly relevant to the breakthrough pressure.

Here, the simple impact pressure calculation at the peak impact force is provided for the estimation of the order of magnitude of the water hammer impact pressure at the

impact velocity around 1 m/s (Table 5.3). The area used for the impact pressure calculation was computed from the diameter in the high-speed camera images at the peak impact force point. We also assumed that the impact pressure on the superhydrophobic textured surface was uniformly distributed on the area under the spreading water droplet and identical to the case of the chemically homogeneous smooth flat surface.

Table 5.3 Impact pressure at the peak impact force point at different impact velocities and on hydrophilic(HP) surface and superhydrophobic (SH) surface.

	Impact velocity = 1.17m/s		Impact velocity = 1.33m/s		Impact velocity = 1.47m/s	
	HP	SH	HP	SH	HP	SH
Impact Pressure (kPa)	11.7	8.19	12.6	9.48	13.4	10.4 (T^* failure)

The impact pressure at the peak impact force point increases when the impact velocity ascends as expected. The difference of impact pressure between the hydrophilic surface case and the superhydrophobic surface case increased because the area in the superhydrophobic surface case was greater than the other case. Interestingly, the Cassie-Baxter state transitioned to the Wenzel state at the impact pressure of around 10 kPa whereas the breakthrough pressure of this superhydrophobic surface is about 40 kPa. This implies (1) that the local impact pressure may be greater than the breakthrough pressure and (2) that the water hammer pressure coefficient α should be around 0.07 at the impact velocity of around 1 m/s, as a consequence of comparison Table 5.3 with Table 5.2.

Chapter 6

6. Conclusion

6.1 Summary and evaluation of thesis objectives

To enhance the robustness of omniphobicity for practical applications, we have explored the role of breakthrough pressure of liquid droplets on omniphobic surfaces and fabrication process in the millimetric and nanometric scale based on three-dimensional printing and various MEMS technology. The breakthrough pressure was investigated further using the software tool Surface Evolver, to better understand the distorted liquid-air interfaces and failure modes of liquid droplets, with the aim of developing a novel *a priori* way for calculating robustness of the omniphobicity. In addition, based on the Surface Evolver simulation results implying five hundred fold increase of breakthrough pressure on the nanometric scale, we have focused on the design and fabrication of nanometric texture. The low cost silicon-based replica molding fabrication process was developed as well as a measurement tool for evaluating the robustness of superoleophobic surfaces against dynamic impact by droplets.

6.2 Future work

Transparent solid surfaces non-wetted with water have recently been highlighted in many studies for a wide range of practical applications including goggles, windshields, and display panels of electronic devices [72]. To increase the ability to maintain the hydrophobicity, which provides self-cleaning effect, the size of texture should be reduced down to submicron scale for daily use. However, regularly arranged polymer-based post texture for satisfying the hydrophobic condition are expected to cause interference problems depending on the period of post arrangement when the submicron period of post structure is near the wavelength of light [73].

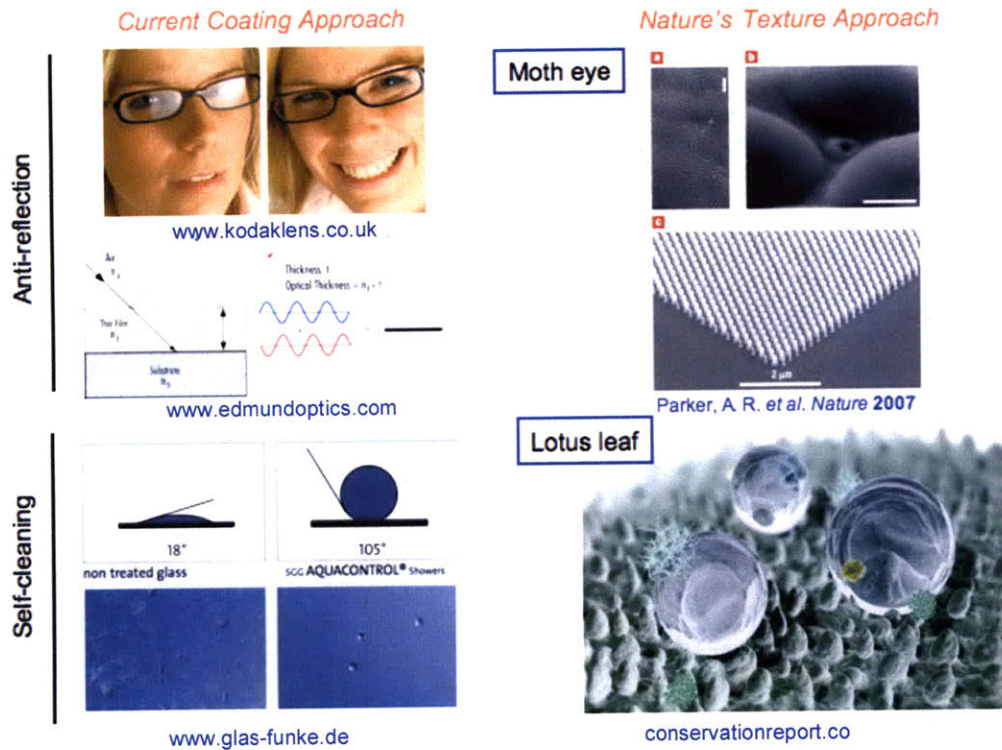


Figure 6.1 Two approaches to achieve anti-reflection and self-cleaning – coating only (left) vs. micro/nanometric surface texture as well as coating (right) [74].

New solutions for challenging problems associated with both solid surface contamination and optics are necessary. For example, dirty displays of cell phones and laptops decrease legibility although the display itself has a high resolution and the necessity of clean displays increases with the advent of touch screen technology. In addition, both the sedimentation of dust and limited unidirectional anti-reflective coating causes a decrease in the efficiency of solar cells. To solve these problems, the integration of different fields related to the nature of the problems should be focused: (1) physico-chemical interaction in adhesion process between different phases and (2) optical principle for the design and fabrication of the functional surfaces. To prevent adhesion

and facilitate separation between solid surfaces and contamination particles, our primary goal is to discover how to employ various nano-texture and surface coating for each specific problem. To delve into the governing mechanisms, we will build on my fundamental knowledge by studying physical chemistry and interfacial fluid mechanics. Furthermore, the study of optics, in addition to my research experience in MEMS, will help to realize one of final objectives: the development of self-cleaning transparent multi-directional anti-reflective surfaces with low cost.

Appendix

// Basic parameters. MKS system is used.

```
parameter Ww      = 0.720 *0.001 // millimeter
parameter Dd      = 0.320 *0.001 // millimeter

parameter Hh      = 0.800 *0.001 // millimeter
parameter Hh_top  = 0.928 *0.001 // millimeter
parameter Hh_bottom = 0.672 *0.001 // millimeter
parameter Hh2     = (0.672-0.1) *0.001 // millimeter
parameter Hh3     = (0.672-0.2) *0.001 // millimeter
parameter Hh4     = (0.672-0.3) *0.001 // millimeter

parameter Rr      = 0.128 *0.001 // millimeter

parameter Tt      = 0.127 *0.001 // millimeter
parameter Tt2     = 0.06 *0.001 // millimeter

parameter DH      = 3 *0.001 //2, 3 millimeter, Droplet Height

parameter volume1 = 10/8 *0.000000001 //0.5, 2 microliter
parameter density1 = 789 // kg/(m^3)

parameter angle   = 60 // contact angle in degrees
parameter tens     = 0.02227 // mN/m
```

```
//SCALE tens fixed
scale_limit 1/tens
//0.0005
```

```
constraint torus_con //clockwise(1/4)
formula: (((x-Ww-Dd)^2+(y-Ww-Dd)^2)^0.5-(Ww-Rr))^2+(z-Hh)^2=Rr^2
```

```
constraint top_con
formula: z=Hh+Tt
```

```
constraint bottom_con
formula: z=Hh-Tt2
```

constraint pillar_con
formula: $(x-Ww-Dd)^2+(y-Ww-Dd)^2=((Ww-Rr)/2)^2$

constraint plate1_con
formula: $z=0$

constraint xmirror_con
formula: $x=0$

constraint ymirror_con
formula: $y=2*(Ww+Dd)$

constraint diagmirror_con
formula: $x=y$

constraint Hh2_con
formula: $z=Hh2$

constraint Hh3_con
formula: $z=Hh3$

constraint Hh4_con
formula: $z=Hh4$

view_transform_generators 8

1 0 0 0 // 1/8 clockwise
0 1 0 0
0 0 1 0
0 0 0 1

-1 0 0 0 // 1/8 clockwise, 2/4 ccw
0 1 0 0
0 0 1 0
0 0 0 1

-1 0 0 0 // 1/8 clockwise
0 -1 0 0 // 3/4 ccw
0 0 1 0
0 0 0 1

1 0 0 0 // 1/8 clockwise
0 -1 0 0 // 4/4 ccw
0 0 1 0

0 0 0 1

0 1 0 0 // 1/8 clockwise

1 0 0 0

0 0 1 0

0 0 0 1

0 -1 0 0 // 1/8 clockwise

1 0 0 0

0 0 1 0

0 0 0 1

0 1 0 0 // 1/8 clockwise

-1 0 0 0

0 0 1 0

0 0 0 1

0 -1 0 0 // 1/8 clockwise

-1 0 0 0

0 0 1 0

0 0 0 1

view_transforms 8

1 0 0 0 // 1/8 clockwise

0 1 0 0

0 0 1 0

0 0 0 1

-1 0 0 0 // 1/8 clockwise, 2/4 ccw

0 1 0 0

0 0 1 0

0 0 0 1

-1 0 0 0 // 1/8 clockwise

0 -1 0 0 // 3/4 ccw

0 0 1 0

0 0 0 1

1 0 0 0 // 1/8 clockwise

0 -1 0 0 // 4/4 ccw

0 0 1 0

0 0 0 1

0 1 0 0 // 1/8 clockwise
1 0 0 0
0 0 1 0
0 0 0 1

0 -1 0 0 // 1/8 clockwise
1 0 0 0
0 0 1 0
0 0 0 1

0 1 0 0 // 1/8 clockwise
-1 0 0 0
0 0 1 0
0 0 0 1

0 -1 0 0 // 1/8 clockwise
-1 0 0 0
0 0 1 0
0 0 0 1

vertices

1 W_w+D_d W_w+D_d H_h+T_t constraints diagmirror_con top_con

2 0 0 0 constraints diagmirror_con xmirror_con

3 $2*(W_w+D_d)$ $2*(W_w+D_d)$ 0 constraints diagmirror_con ymirror_con

4 0 $2*(W_w+D_d)$ 0 constraints ymirror_con xmirror_con

11 $W_w+D_d+0.5*(0.7*W_w)$ $W_w+D_d+0.5*(0.7*W_w)$ H_h+T_t constraints diagmirror_con top_con

12 W_w+D_d $W_w+D_d+0.5*(W_w)$ H_h+T_t constraints top_con

13 $W_w+D_d-0.5*(0.4*W_w)$ $W_w+D_d+0.5*(0.9*W_w)$ H_h+T_t constraints top_con

14 $W_w+D_d-0.5*(0.7*W_w)$ $W_w+D_d+0.5*(0.7*W_w)$ H_h+T_t constraints top_con

15 $W_w+D_d-0.5*(0.9*W_w)$ $W_w+D_d+0.5*(0.4*W_w)$ H_h+T_t constraints top_con

16 $W_w+D_d-0.5*(W_w)$ W_w+D_d H_h+T_t constraints top_con

17 $W_w+D_d-0.5*(0.7*W_w)$ $W_w+D_d-0.5*(0.7*W_w)$ H_h+T_t constraints diagmirror_con top_con

21 $W_w+D_d+0.7*(0.7*W_w)$ $W_w+D_d+0.7*(0.7*W_w)$ H_h+T_t constraints diagmirror_con top_con torus_con

22 W_w+D_d $W_w+D_d+0.7*(W_w)$ H_h+T_t constraints top_con torus_con

23 $W_w+D_d-0.7*(0.4*W_w)$ $W_w+D_d+0.7*(0.9*W_w)$ H_h+T_t constraints top_con torus_con

24 $W_w+D_d-0.7*(0.7*W_w)$ $W_w+D_d+0.7*(0.7*W_w)$ Hh+Tt constraints top_con
 torus_con
 25 $W_w+D_d-0.7*(0.9*W_w)$ $W_w+D_d+0.7*(0.4*W_w)$ Hh+Tt constraints top_con
 torus_con
 26 $W_w+D_d-0.7*(W_w)$ W_w+D_d Hh+Tt constraints top_con torus_con
 27 $W_w+D_d-0.7*(0.7*W_w)$ $W_w+D_d-0.7*(0.7*W_w)$ Hh+Tt constraints diagmirror_con
 top_con torus_con

 31 $W_w+D_d+0.9*0.7*W_w$ $W_w+D_d+0.9*(0.7*W_w)$ Hh+Tt constraints diagmirror_con
 torus_con
 32 W_w+D_d $W_w+D_d+0.9*(W_w)$ Hh+Tt constraints torus_con
 33 $W_w+D_d-0.9*0.4*W_w$ $W_w+D_d+0.9*(0.9*W_w)$ Hh+Tt constraints torus_con
 34 $W_w+D_d-0.9*0.7*W_w$ $W_w+D_d+0.9*(0.7*W_w)$ Hh+Tt constraints torus_con
 35 $W_w+D_d-0.9*0.9*W_w$ $W_w+D_d+0.9*(0.4*W_w)$ Hh+Tt constraints torus_con
 36 $W_w+D_d-0.9*W_w$ W_w+D_d Hh+Tt constraints torus_con
 37 $W_w+D_d-0.9*0.7*W_w$ $W_w+D_d-0.9*(0.7*W_w)$ Hh+Tt constraints diagmirror_con
 torus_con

 41 $W_w+D_d+0.7*(W_w)$ $W_w+D_d+0.7*(W_w)$ Hh constraints diagmirror_con torus_con
 42 W_w+D_d $W_w+D_d+(W_w)$ Hh constraints torus_con
 43 $W_w+D_d-0.4*(W_w)$ $W_w+D_d+0.9*(W_w)$ Hh constraints torus_con
 44 $W_w+D_d-0.7*(W_w)$ $W_w+D_d+0.7*(W_w)$ Hh constraints torus_con
 45 $W_w+D_d-0.9*(W_w)$ $W_w+D_d+0.4*(W_w)$ Hh constraints torus_con
 46 $W_w+D_d-(W_w)$ W_w+D_d Hh constraints torus_con
 47 $W_w+D_d-0.7*(W_w)$ $W_w+D_d-0.7*(W_w)$ Hh constraints diagmirror_con torus_con

 101 W_w+D_d W_w+D_d Hh-Tt2 constraints diagmirror_con bottom_con

 111 $W_w+D_d+0.5*(0.7*W_w)$ $W_w+D_d+0.5*(0.7*W_w)$ Hh-Tt2 constraints
 diagmirror_con bottom_con pillar_con
 112 W_w+D_d $W_w+D_d+0.5*(W_w)$ Hh-Tt2 constraints bottom_con pillar_con
 113 $W_w+D_d-0.5*(0.4*W_w)$ $W_w+D_d+0.5*(0.9*W_w)$ Hh-Tt2 constraints bottom_con
 pillar_con
 114 $W_w+D_d-0.5*(0.7*W_w)$ $W_w+D_d+0.5*(0.7*W_w)$ Hh-Tt2 constraints bottom_con
 pillar_con
 115 $W_w+D_d-0.5*(0.9*W_w)$ $W_w+D_d+0.5*(0.4*W_w)$ Hh-Tt2 constraints bottom_con
 pillar_con
 116 $W_w+D_d-0.5*(W_w)$ W_w+D_d Hh-Tt2 constraints bottom_con pillar_con
 117 $W_w+D_d-0.5*(0.7*W_w)$ $W_w+D_d-0.5*(0.7*W_w)$ Hh-Tt2 constraints
 diagmirror_con bottom_con pillar_con

 121 $W_w+D_d+0.7*(0.7*W_w)$ $W_w+D_d+0.7*(0.7*W_w)$ Hh-Tt2 constraints
 diagmirror_con bottom_con torus_con
 122 W_w+D_d $W_w+D_d+0.7*(W_w)$ Hh-Tt2 constraints bottom_con torus_con

123 $Ww+Dd-0.7*(0.4*Ww)$ $Ww+Dd+0.7*(0.9*Ww)$ Hh-Tt2 constraints bottom_con
torus_con
124 $Ww+Dd-0.7*(0.7*Ww)$ $Ww+Dd+0.7*(0.7*Ww)$ Hh-Tt2 constraints bottom_con
torus_con
125 $Ww+Dd-0.7*(0.9*Ww)$ $Ww+Dd+0.7*(0.4*Ww)$ Hh-Tt2 constraints bottom_con
torus_con
126 $Ww+Dd-0.7*(Ww)$ $Ww+Dd$ Hh-Tt2 constraints bottom_con torus_con
127 $Ww+Dd-0.7*(0.7*Ww)$ $Ww+Dd-0.7*(0.7*Ww)$ Hh-Tt2 constraints
diagmirror_con bottom_con torus_con

131 $Ww+Dd+0.9*0.7*Ww$ $Ww+Dd+0.9*0.7*Ww$ Hh-Tt2 constraints diagmirror_con
torus_con
132 $Ww+Dd$ $Ww+Dd+0.9*Ww$ Hh-Tt2 constraints torus_con
133 $Ww+Dd-0.9*0.4*Ww$ $Ww+Dd+0.9*0.9*Ww$ Hh-Tt2 constraints torus_con
134 $Ww+Dd-0.9*0.7*Ww$ $Ww+Dd+0.9*0.7*Ww$ Hh-Tt2 constraints torus_con
135 $Ww+Dd-0.9*0.9*Ww$ $Ww+Dd+0.9*0.4*Ww$ Hh-Tt2 constraints torus_con
136 $Ww+Dd-0.9*Ww$ $Ww+Dd$ Hh-Tt2 constraints torus_con
137 $Ww+Dd-0.9*0.7*Ww$ $Ww+Dd-0.9*0.7*Ww$ Hh-Tt2 constraints diagmirror_con
torus_con

501 0 0 DH constraints diagmirror_con xmirror_con
502 $Ww+Dd$ $Ww+Dd$ DH constraints diagmirror_con
503 0 $Ww+Dd$ DH constraints xmirror_con

551 0 0 Hh-Tt2 constraints diagmirror_con xmirror_con
553 0 $Ww+Dd$ Hh-Tt2 constraints xmirror_con

611 $Ww+Dd+0.5*(0.7*Ww)$ $Ww+Dd+0.5*(0.7*Ww)$ Hh/2 constraints diagmirror_con
pillar_con
612 $Ww+Dd$ $Ww+Dd+0.5*(Ww)$ Hh/2 constraints pillar_con
613 $Ww+Dd-0.5*(0.4*Ww)$ $Ww+Dd+0.5*(0.9*Ww)$ Hh/2 constraints pillar_con
614 $Ww+Dd-0.5*(0.7*Ww)$ $Ww+Dd+0.5*(0.7*Ww)$ Hh/2 constraints pillar_con
615 $Ww+Dd-0.5*(0.9*Ww)$ $Ww+Dd+0.5*(0.4*Ww)$ Hh/2 constraints pillar_con
616 $Ww+Dd-0.5*(Ww)$ $Ww+Dd$ Hh/2 constraints pillar_con
617 $Ww+Dd-0.5*(0.7*Ww)$ $Ww+Dd-0.5*(0.7*Ww)$ Hh/2 constraints diagmirror_con
pillar_con

711 $Ww+Dd+0.5*(0.7*Ww)$ $Ww+Dd+0.5*(0.7*Ww)$ 0 constraints diagmirror_con
plate1_con pillar_con
712 $Ww+Dd$ $Ww+Dd+0.5*(Ww)$ 0 constraints plate1_con pillar_con
713 $Ww+Dd-0.5*(0.4*Ww)$ $Ww+Dd+0.5*(0.9*Ww)$ 0 constraints plate1_con
pillar_con
714 $Ww+Dd-0.5*(0.7*Ww)$ $Ww+Dd+0.5*(0.7*Ww)$ 0 constraints plate1_con
pillar_con

715 $Ww+Dd-0.5*(0.9*Ww)$ $Ww+Dd+0.5*(0.4*Ww)$ 0 constraints plate1_con
 pillar_con
 716 $Ww+Dd-0.5*(Ww)$ $Ww+Dd$ 0 constraints plate1_con pillar_con
 717 $Ww+Dd-0.5*(0.7*Ww)$ $Ww+Dd-0.5*(0.7*Ww)$ 0 constraints diagmirror_con
 plate1_con pillar_con

edges

1 1 11 constraints diagmirror_con top_con
 2 1 12 constraints top_con
 3 1 13 constraints top_con
 4 1 14 constraints top_con
 5 1 15 constraints top_con
 6 1 16 constraints top_con
 7 1 17 constraints diagmirror_con top_con

 11 11 21 constraints diagmirror_con top_con
 12 12 22 constraints top_con
 13 13 23 constraints top_con
 14 14 24 constraints top_con
 15 15 25 constraints top_con
 16 16 26 constraints top_con
 17 17 27 constraints diagmirror_con top_con

 21 21 31 constraints diagmirror_con torus_con
 22 22 32 constraints torus_con
 23 23 33 constraints torus_con
 24 24 34 constraints torus_con
 25 25 35 constraints torus_con
 26 26 36 constraints torus_con
 27 27 37 constraints diagmirror_con torus_con

 31 31 41 constraints diagmirror_con torus_con
 32 32 42 constraints torus_con
 33 33 43 constraints torus_con
 34 34 44 constraints torus_con
 35 35 45 constraints torus_con
 36 36 46 constraints torus_con
 37 37 47 constraints diagmirror_con torus_con

 101 101 111 constraints diagmirror_con bottom_con
 102 101 112 constraints bottom_con
 103 101 113 constraints bottom_con

104 101 114 constraints bottom_con
105 101 115 constraints bottom_con
106 101 116 constraints bottom_con
107 101 117 constraints diagmirror_con bottom_con

111 111 121 constraints diagmirror_con bottom_con
112 112 122 constraints bottom_con
113 113 123 constraints bottom_con
114 114 124 constraints bottom_con
115 115 125 constraints bottom_con
116 116 126 constraints bottom_con
117 117 127 constraints diagmirror_con bottom_con

121 121 131 constraints diagmirror_con torus_con
122 122 132 constraints torus_con
123 123 133 constraints torus_con
124 124 134 constraints torus_con
125 125 135 constraints torus_con
126 126 136 constraints torus_con
127 127 137 constraints diagmirror_con torus_con

131 131 41 constraints diagmirror_con torus_con
132 132 42 constraints torus_con
133 133 43 constraints torus_con
134 134 44 constraints torus_con
135 135 45 constraints torus_con
136 136 46 constraints torus_con
137 137 47 constraints diagmirror_con torus_con

211 11 12 constraints top_con
212 12 13 constraints top_con
213 13 14 constraints top_con
214 14 15 constraints top_con
215 15 16 constraints top_con
216 16 17 constraints top_con

221 21 22 constraints top_con torus_con
222 22 23 constraints top_con torus_con
223 23 24 constraints top_con torus_con
224 24 25 constraints top_con torus_con
225 25 26 constraints top_con torus_con
226 26 27 constraints top_con torus_con

231 31 32 constraints torus_con
232 32 33 constraints torus_con

233 33 34 constraints torus_con
234 34 35 constraints torus_con
235 35 36 constraints torus_con
236 36 37 constraints torus_con

241 41 42 constraints torus_con
242 42 43 constraints torus_con
243 43 44 constraints torus_con
244 44 45 constraints torus_con
245 45 46 constraints torus_con
246 46 47 constraints torus_con

311 111 112 constraints bottom_con pillar_con
312 112 113 constraints bottom_con pillar_con
313 113 114 constraints bottom_con pillar_con
314 114 115 constraints bottom_con pillar_con
315 115 116 constraints bottom_con pillar_con
316 116 117 constraints bottom_con pillar_con

321 121 122 constraints bottom_con torus_con
322 122 123 constraints bottom_con torus_con
323 123 124 constraints bottom_con torus_con
324 124 125 constraints bottom_con torus_con
325 125 126 constraints bottom_con torus_con
326 126 127 constraints bottom_con torus_con

331 131 132 constraints torus_con
332 132 133 constraints torus_con
333 133 134 constraints torus_con
334 134 135 constraints torus_con
335 135 136 constraints torus_con
336 136 137 constraints torus_con

501 501 502 constraints diagmirror_con
502 502 503
503 503 501 constraints xmirror_con

504 502 11 constraints diagmirror_con
505 503 553 constraints xmirror_con

520 2 3 constraints diagmirror_con
530 3 4 constraints ymirror_con
540 4 2 constraints xmirror_con

551 551 47 constraints diagmirror_con

552 45 553
553 553 551 constraints xmirror_con

611 611 612 constraints pillar_con
612 612 613 constraints pillar_con
613 613 614 constraints pillar_con
614 614 615 constraints pillar_con
615 615 616 constraints pillar_con
616 616 617 constraints pillar_con

621 111 611 constraints diagmirror_con pillar_con
622 112 612 constraints pillar_con
623 113 613 constraints pillar_con
624 114 614 constraints pillar_con
625 115 615 constraints pillar_con
626 116 616 constraints pillar_con
627 117 617 constraints diagmirror_con pillar_con

711 711 712 constraints pillar_con plate1_con
712 712 713 constraints pillar_con plate1_con
713 713 714 constraints pillar_con plate1_con
714 714 715 constraints pillar_con plate1_con
715 715 716 constraints pillar_con plate1_con
716 716 717 constraints pillar_con plate1_con

721 611 711 constraints diagmirror_con pillar_con
722 612 712 constraints pillar_con
723 613 713 constraints pillar_con
724 614 714 constraints pillar_con
725 615 715 constraints pillar_con
726 616 716 constraints pillar_con
727 617 717 constraints diagmirror_con pillar_con

faces

1 1 211 -2 constraints top_con tension tens*0.5*(1-cos(angle*pi/180)) color blue
2 2 212 -3 constraints top_con tension tens*0.5*(1-cos(angle*pi/180)) color blue
3 3 213 -4 constraints top_con tension tens*0.5*(1-cos(angle*pi/180)) color blue
4 4 214 -5 constraints top_con tension tens*0.5*(1-cos(angle*pi/180)) color blue
5 5 215 -6 constraints top_con tension tens*0.5*(1-cos(angle*pi/180)) color blue
6 6 216 -7 constraints top_con tension tens*0.5*(1-cos(angle*pi/180)) color blue

11 11 221 -12 -211 constraints top_con tension tens*0.5*(1+cos(angle*pi/180)) color red
12 12 222 -13 -212 constraints top_con tension tens*0.5*(1+cos(angle*pi/180)) color red
13 13 223 -14 -213 constraints top_con tension tens*0.5*(1+cos(angle*pi/180)) color red
14 14 224 -15 -214 constraints top_con tension tens*0.5*(1+cos(angle*pi/180)) color red
15 15 225 -16 -215 constraints top_con tension tens*0.5*(1-cos(angle*pi/180)) color blue
16 16 226 -17 -216 constraints top_con tension tens*0.5*(1-cos(angle*pi/180)) color blue

21 21 231 -22 -221 constraints torus_con tension tens*0.5*(1+cos(angle*pi/180)) color red
22 22 232 -23 -222 constraints torus_con tension tens*0.5*(1+cos(angle*pi/180)) color red
23 23 233 -24 -223 constraints torus_con tension tens*0.5*(1+cos(angle*pi/180)) color red
24 24 234 -25 -224 constraints torus_con tension tens*0.5*(1+cos(angle*pi/180)) color red
25 25 235 -26 -225 constraints torus_con tension tens*0.5*(1-cos(angle*pi/180)) color blue
26 26 236 -27 -226 constraints torus_con tension tens*0.5*(1-cos(angle*pi/180)) color blue

31 31 241 -32 -231 constraints torus_con tension tens*0.5*(1+cos(angle*pi/180)) color red
32 32 242 -33 -232 constraints torus_con tension tens*0.5*(1+cos(angle*pi/180)) color red
33 33 243 -34 -233 constraints torus_con tension tens*0.5*(1+cos(angle*pi/180)) color red
34 34 244 -35 -234 constraints torus_con tension tens*0.5*(1+cos(angle*pi/180)) color red
35 35 245 -36 -235 constraints torus_con tension tens*0.5*(1-cos(angle*pi/180)) color blue
36 36 246 -37 -236 constraints torus_con tension tens*0.5*(1-cos(angle*pi/180)) color blue

101 101 311 -102 constraints bottom_con tension tens*0.5*(1+cos(angle*pi/180)) color red
102 102 312 -103 constraints bottom_con tension tens*0.5*(1+cos(angle*pi/180)) color red
103 103 313 -104 constraints bottom_con tension tens*0.5*(1+cos(angle*pi/180)) color red
104 104 314 -105 constraints bottom_con tension tens*0.5*(1+cos(angle*pi/180)) color red
105 105 315 -106 constraints bottom_con tension tens*0.5*(1+cos(angle*pi/180)) color red
106 106 316 -107 constraints bottom_con tension tens*0.5*(1+cos(angle*pi/180)) color red

111 111 321 -112 -311 constraints bottom_con tension tens*0.5*(1+cos(angle*pi/180))
color red
112 112 322 -113 -312 constraints bottom_con tension tens*0.5*(1+cos(angle*pi/180))
color red
113 113 323 -114 -313 constraints bottom_con tension tens*0.5*(1+cos(angle*pi/180))
color red
114 114 324 -115 -314 constraints bottom_con tension tens*0.5*(1+cos(angle*pi/180))
color red
115 115 325 -116 -315 constraints bottom_con tension tens*0.5*(1+cos(angle*pi/180))
color red
116 116 326 -117 -316 constraints bottom_con tension tens*0.5*(1+cos(angle*pi/180))
color red

121 121 331 -122 -321 constraints torus_con tension tens*0.5*(1+cos(angle*pi/180))
color red
122 122 332 -123 -322 constraints torus_con tension tens*0.5*(1+cos(angle*pi/180))
color red
123 123 333 -124 -323 constraints torus_con tension tens*0.5*(1+cos(angle*pi/180))
color red
124 124 334 -125 -324 constraints torus_con tension tens*0.5*(1+cos(angle*pi/180))
color red
125 125 335 -126 -325 constraints torus_con tension tens*0.5*(1+cos(angle*pi/180))
color red
126 126 336 -127 -326 constraints torus_con tension tens*0.5*(1+cos(angle*pi/180))
color red

131 131 241 -132 -331 constraints torus_con tension tens*0.5*(1+cos(angle*pi/180))
color red
132 132 242 -133 -332 constraints torus_con tension tens*0.5*(1+cos(angle*pi/180))
color red
133 133 243 -134 -333 constraints torus_con tension tens*0.5*(1+cos(angle*pi/180))
color red
134 134 244 -135 -334 constraints torus_con tension tens*0.5*(1+cos(angle*pi/180))
color red
135 135 245 -136 -335 constraints torus_con tension tens*0.5*(1+cos(angle*pi/180))
color red
136 136 246 -137 -336 constraints torus_con tension tens*0.5*(1+cos(angle*pi/180))
color red

501 501 502 503 tension tens color blue
502 504 211 212 213 214 15 25 35 552 -505 -502 tension tens color blue
520 520 530 540 no_refine color red
551 551 -246 -245 552 553 tension tens color blue


```

611 611 -622 -311 621 constraints pillar_con tension tens*0.5*(1+cos(angle*pi/180))
color red
612 612 -623 -312 622 constraints pillar_con tension tens*0.5*(1+cos(angle*pi/180))
color red
613 613 -624 -313 623 constraints pillar_con tension tens*0.5*(1+cos(angle*pi/180))
color red
614 614 -625 -314 624 constraints pillar_con tension tens*0.5*(1+cos(angle*pi/180))
color red
615 615 -626 -315 625 constraints pillar_con tension tens*0.5*(1+cos(angle*pi/180))
color red
616 616 -627 -316 626 constraints pillar_con tension tens*0.5*(1+cos(angle*pi/180))
color red

```

```

711 711 -722 -611 721 constraints pillar_con tension tens*0.5*(1+cos(angle*pi/180))
color red
712 712 -723 -612 722 constraints pillar_con tension tens*0.5*(1+cos(angle*pi/180))
color red
713 713 -724 -613 723 constraints pillar_con tension tens*0.5*(1+cos(angle*pi/180))
color red
714 714 -725 -614 724 constraints pillar_con tension tens*0.5*(1+cos(angle*pi/180))
color red
715 715 -726 -615 725 constraints pillar_con tension tens*0.5*(1+cos(angle*pi/180))
color red
716 716 -727 -616 726 constraints pillar_con tension tens*0.5*(1+cos(angle*pi/180))
color red

```

bodies

```
1 501 502 -1 -2 -3 -4 -5 -6 -15 -16 -25 -26 -35 -36 -551 volume volume1 density density1
```

read

```

// typical evolution
gogo := {
set background white;
  show facet where color!= yellow;
  // show edge where original==14 or valence != 2;

r; r; g 20; r; u; t 0.00003; g 20; hessian_seek; hessian_seek; V; V; V;
g 20; G 9.8; hessian_seek; hessian_seek;V; V;

```

```
g 20; G 9.8; hessian_seek; hessian_seek;V; V;  
g 20; G 9.8; hessian_seek; hessian_seek;V; V;  
g 20; G 9.8; hessian_seek; hessian_seek;V; V;  
g 20; G 9.8; hessian_seek; hessian_seek;V; V;  
g 20; G 9.8; hessian_seek; hessian_seek;V; V;
```

```
g 10;  
hessian_seek;
```

```
g 20;  
hessian_seek;  
hessian_seek;
```

```
printf "Angle: %3.0f Reference point: %f\n Reference point: %f\n Lowest  
point: %f\n",angle,min(vertex[15],z),min(vertex[17],z),min(vertex where not fixed,z);
```

```
}
```

Bibliography

- [1] A. Lafuma, D. Quere, Superhydrophobic states, *Nature Materials* 2 (2003) 457-460.
- [2] D. Quere, Non-sticking drops, *Reports on Progress in Physics* 68 (2005) 2495-2532.
- [3] P.G.d. Gennes, Wetting: statics and dynamics, *Reviews of Modern Physics* 57 (1985) 827-863.
- [4] L. Feng, S.H. Li, Y.S. Li, H.J. Li, L.J. Zhang, J. Zhai, Y.L. Song, B.Q. Liu, L. Jiang, D.B. Zhu, Super-hydrophobic surfaces: From natural to artificial, *Advanced Materials* 14 (2002) 1857-1860.
- [5] W. Barthlott, C. Neinhuis, Purity of the sacred lotus, or escape from contamination in biological surfaces, *Planta* 202 (1997) 1-8.
- [6] A. Marmur, The lotus effect: Superhydrophobicity and metastability, *Langmuir* 20 (2004) 3517-3519.
- [7] N.A. Patankar, Mimicking the lotus effect: Influence of double roughness structures and slender pillars, *Langmuir* 20 (2004) 8209-8213.
- [8] A. Tuteja, W. Choi, M.L. Ma, J.M. Mabry, S.A. Mazzella, G.C. Rutledge, G.H. McKinley, R.E. Cohen, Designing superoleophobic surfaces, *Science* 318 (2007) 1618-1622.
- [9] M. Callies, D. Quere, On water repellency, *Soft Matter* 1 (2005) 55-61.
- [10] R.E. Johnson, R.H. Dettre, Contact Angle Hysteresis. I. Study of an Idealized Rough Surface, American Chemical Society, Washington, DC, 1964.
- [11] R.E. Dettre, R.H. Johnson, Contact Angle Hysteresis. II. Contact Angle Measurements on Rough Surfaces, American Chemical Society, Washington, DC, 1964.
- [12] R. Furstner, W. Barthlott, C. Neinhuis, P. Walzel, Wetting and self-cleaning properties of artificial superhydrophobic surfaces, *Langmuir* 21 (2005) 956-961.
- [13] V.A. Lifton, J.A. Taylor, B. Vyas, P. Kolodner, R. Cirelli, N. Basavanahally, A. Papazian, R. Frahm, S. Simon, T. Krupenkin, Superhydrophobic membranes with electrically controllable permeability and their application to "smart" microbatteries, *Applied Physics Letters* 93 (2008) -.
- [14] D. Quere, Wetting and roughness, *Annual Review of Materials Research* 38 (2008) 71-99.
- [15] M. Nosonovsky, B. Bhushan, Biomimetic superhydrophobic surfaces: Multiscale approach, *Nano Letters* 7 (2007) 2633-2637.
- [16] C. Dorrer, J. Ruhe, Some thoughts on superhydrophobic wetting, *Soft Matter* 5 (2009) 51-61.
- [17] S.A. Brewer, C.R. Willis, Structure and oil repellency: textiles with liquid repellency to hexane, *Applied Surface Science* 254 (2008) 6450-6454.
- [18] J. Bico, U. Thiele, D. Quere, Wetting of textured surfaces, *Colloids and Surfaces a-Physicochemical and Engineering Aspects* 206 (2002) 41-46.
- [19] A. Marmur, Wetting on hydrophobic rough surfaces: To be heterogeneous or not to be?, *Langmuir* 19 (2003) 8343-8348.

- [20] C.W. Extrand, Model for contact angles and hysteresis on rough and ultraphobic surfaces, *Langmuir* 18 (2002) 7991-7999.
- [21] Z. Burton, B. Bhushan, Hydrophobicity, adhesion, and friction properties of nanopatterned polymers and scale dependence for micro- and nanoelectromechanical systems, *Nano Letters* 5 (2005) 1607-1613.
- [22] K.K.S. Lau, J. Bico, K.B.K. Teo, M. Chhowalla, G.A.J. Amaratunga, W.I. Milne, G.H. McKinley, K.K. Gleason, Superhydrophobic carbon nanotube forests, *Nano Letters* 3 (2003) 1701-1705.
- [23] J.P. Youngblood, T.J. McCarthy, Ultrahydrophobic polymer surfaces prepared by simultaneous ablation of polypropylene and sputtering of poly(tetrafluoroethylene) using radio frequency plasma, *Macromolecules* 32 (1999) 6800-6806.
- [24] B. Bhushan, Y.C. Jung, Natural and biomimetic artificial surfaces for superhydrophobicity, self-cleaning, low adhesion, and drag reduction, *Progress in Materials Science* 56 (2011) 1-108.
- [25] Y.T. Cheng, D.E. Rodak, C.A. Wong, C.A. Hayden, Effects of micro- and nanostructures on the self-cleaning behaviour of lotus leaves, *Nanotechnology* 17 (2006) 1359-1362.
- [26] S. Shibuichi, T. Yamamoto, T. Onda, K. Tsujii, Super water- and oil-repellent surfaces resulting from fractal structure, *Journal of Colloid and Interface Science* 208 (1998) 287-294.
- [27] A. Tuteja, W. Choi, G.H. McKinley, R.E. Cohen, M.F. Rubner, Design Parameters for Superhydrophobicity and Superoleophobicity (vol 33, pg 757, 2008), *Mrs Bulletin* 33 (2008) 996-996.
- [28] A. Tuteja, W. Choi, J.M. Mabry, G.H. McKinley, R.E. Cohen, Robust omniphobic surfaces, *Proc Natl Acad Sci U S A* 105 (2008) 18200-18205.
- [29] K. Tsujii, T. Yamamoto, T. Onda, S. Shibuichi, Super oil-repellent surfaces, *Angewandte Chemie-International Edition in English* 36 (1997) 1011-1012.
- [30] A. Ahuja, J.A. Taylor, V. Lifton, A.A. Sidorenko, T.R. Salamon, E.J. Lobaton, P. Kolodner, T.N. Krupenkin, Nanonails: A simple geometrical approach to electrically tunable superlyophobic surfaces, *Langmuir* 24 (2008) 9-14.
- [31] T. Young, An Essay on the Cohesion of Fluids, *Philosophical Transactions of the Royal Society of London* (1805) 65-87.
- [32] E.G. Shafrin, W.A. Zisman, Upper Limits to the Contact Angles of Liquids on Solids, American Chemical Society, Washington DC, 1964.
- [33] A.B.D. Cassie, S. Baxter, Wettability of porous surfaces., *Transactions of the Faraday Society* 40 (1944) 0546-0550.
- [34] R.N. Wenzel, Resistance of solid surfaces to wetting by water, *Industrial and Engineering Chemistry* 28 (1936) 988-994.
- [35] S. Herminghaus, Roughness-induced non-wetting, *Europhysics Letters* 52 (2000) 165-170.
- [36] L.L. Cao, H.H. Hu, D. Gao, Design and fabrication of micro-textures for inducing a superhydrophobic behavior on hydrophilic materials, *Langmuir* 23 (2007) 4310-4314.

- [37] L.L. Cao, T.P. Price, M. Weiss, D. Gao, Super water- and oil-repellent surfaces on intrinsically hydrophilic and oleophilic porous silicon films, *Langmuir* 24 (2008) 1640-1643.
- [38] J.L. Liu, X.Q. Feng, G.F. Wang, S.W. Yu, Mechanisms of superhydrophobicity on hydrophilic substrates, *Journal of Physics-Condensed Matter* 19 (2007) -.
- [39] C.W. Extrand, Criteria for ultralyophobic surfaces, *Langmuir* 20 (2004) 5013-5018.
- [40] M. Nosonovsky, Multiscale roughness and stability of superhydrophobic biomimetic interfaces, *Langmuir* 23 (2007) 3157-3161.
- [41] A. Marmur, From hydrophilic to superhydrophobic: Theoretical conditions for making high-contact-angle surfaces from low-contact-angle materials, *Langmuir* 24 (2008) 7573-7579.
- [42] T. Onda, S. Shibuichi, N. Satoh, K. Tsujii, Super-water-repellent fractal surfaces, *Langmuir* 12 (1996) 2125-2127.
- [43] L. Barbieri, E. Wagner, P. Hoffmann, Water wetting transition parameters of perfluorinated substrates with periodically distributed flat-top microscale obstacles, *Langmuir* 23 (2007) 1723-1734.
- [44] C. Dorrer, J. Ruhe, Condensation and wetting transitions on microstructured ultrahydrophobic surfaces, *Langmuir* 23 (2007) 3820-3824.
- [45] N.A. Patankar, Transition between superhydrophobic states on rough surfaces, *Langmuir* 20 (2004) 7097-7102.
- [46] D. Bartolo, F. Bouamrène, E. Verneuil, A. Buguin, P. Silberzan, S. Moulinet, Bouncing or sticky droplets: Impalement transitions on superhydrophobic micropatterned surfaces, *Europhysics Letters* 74 (2006) 299-305.
- [47] A. Dupuis, J.M. Yeomans, Modeling droplets on superhydrophobic surfaces: Equilibrium states and transitions, *Langmuir* 21 (2005) 2624-2629.
- [48] H. Kusumaatmaja, M.L. Blow, A. Dupuis, J.M. Yeomans, The collapse transition on superhydrophobic surfaces, *Europhysics Letters* 81 (2008) 36003.
- [49] Q.S. Zheng, Y. Yu, Z.H. Zhao, Effects of hydraulic pressure on the stability and transition of wetting modes of superhydrophobic surfaces, *Langmuir* 21 (2005) 12207-12212.
- [50] E.J. Lobaton, T.R. Salamon, Computation of constant mean curvature surfaces: Application to the gas-liquid interface of a pressurized fluid on a superhydrophobic surface, *Journal of Colloid and Interface Science* 314 (2007) 184-198.
- [51] A.L. Yarin, Drop impact dynamics: Splashing, spreading, receding, bouncing... *Annual Review of Fluid Mechanics* 38 (2006) 159-192.
- [52] S.S. Cook, Erosion by water-hammer, *Proceedings of the Royal Society of London. Series A, Containing Papers of a Mathematical Physical Character* 119 (1928) 481-488.
- [53] O.G. Engel, Waterdrop Collisions with Solid Surfaces, *Journal of Research of the National Bureau of Standards* 54 (1955) 281-298.
- [54] O.G. Engel, Note on Particle Velocity in Collisions between Liquid Drops and Solids, *Journal of Research of the National Bureau of Standards Section a-Physics and Chemistry* 64 (1960) 497-498.

- [55] M.A. Nearing, J.M. Bradford, R.D. Holtz, Measurement of force vs. time relation for waterdrop impact, *Soil Society of America Journal* 50 (1986) 1532-1536.
- [56] M.A. Nearing, J.M. Bradford, R.D. Holtz, Measurement of waterdrop impact pressures on soil surfaces, *Soil Society of America Journal* 51 (1987) 1302-1306.
- [57] T. Deng, K.K. Varanasi, M. Hsu, N. Bhate, C. Keimel, J. Stein, M. Blohm, Nonwetting of impinging droplets on textured surfaces, *Applied Physics Letters* 94 (2009) 133109.
- [58] W. Choi, A. Tuteja, S. Chhatre, J.M. Mabry, R.E. Cohen, G.H. McKinley, Fabrics with Tunable Oleophobicity, *Advanced Materials* 21 (2009) 2190-+.
- [59] H.F. Hoefnagels, D. Wu, G. deWith, W. Ming, Biomimetic superhydrophobic and highly oleophobic cotton textiles, *Langmuir* 23 (2007) 13158-13163.
- [60] S.S. Chhatre, W. Choi, A. Tuteja, K.C. Park, J.M. Mabry, G.H. McKinley, R.E. Cohen, Scale Dependence of Omniphobic Mesh Surfaces, *Langmuir* (2009).
- [61] C. Ybert, C. Barentin, C. Cottin-Bizonne, P. Joseph, L. Bocquet, Achieving large slip with superhydrophobic surfaces: scaling laws for generic geometries, *Physics of Fluids* 19 (2007) 123601.
- [62] A.M.J. Davis, E. Lauga, The friction of a mesh-like super-hydrophobic surface, *Physics of Fluids* 21 (2009) 113101.
- [63] C.-H. Choi, C.-J. Kim, Large slip of aqueous liquid flow over a nanoengineered superhydrophobic surface, *Physics Review Letters* 96 (2006) 066001.
- [64] C. Lee, C.-H. Choi, C.-J. Kim, Structured surfaces for a giant liquid slip, *Physics Review Letters* 101 (2008) 064501.
- [65] Y.C. Jung, B. Bhushan, Dynamic effects of bouncing water droplets on superhydrophobic surfaces, *Langmuir* 24 (2008) 6262-6269.
- [66] K.A. Brakke, *The Motion of a Surface by Its Mean Curvature*, Princeton University Press, Princeton, 1977.
- [67] K.A. Brakke, *The Surface Evolver*, 2003.
- [68] D.C. Roux, J.J. Cooper-White, G.H. McKinley, V. Tirtaatmadja, Drop impact of Newtonian and elastic fluids, *Physics of Fluids* 15 (2003) S12.
- [69] R. Rioboo, C. Tropea, M. Marengo, Outcomes from a drop impact on solid surfaces, *Atomization and Sprays* 11 (2001).
- [70] J.A. Caskey, W.B.J. Barlage, An improved experimental technique for determining dynamic surface tension of water and surfactant solutions, *Journal of Colloid and Interface Science* 35 (1971) 46-52.
- [71] A.S. Grinspan, R. Gnanamoorthy, Impact force of low velocity liquid droplets measured using piezoelectric PVDF film, *Colloids and Surface A: Physicochemical and Engineering Aspects* 356 (2010) 162-168.
- [72] F. Xia, L. Jiang, Bio-inspired, smart, multiscale interfacial materials, *Advanced Materials* 20 (2008) 2842-2858.
- [73] E. Hecht, *Optics*, 4th ed., Pearson Education, Inc., San Francisco, 2002.
- [74] A.R. Parker, H.E. Townley, Biomimetics of photonic nanostructures, *Nat Nanotechnol* 2 (2007) 347-353.